Light cone distribution amplitude for the Λ baryon from lattice QCD

Min-Huan Chu,[1,2,3] Haoyang Bai,[4,5] Jun Hua,[6,7,*] Jian Liang,[6,7] Xiangdong Ji,[8] Andreas Schäfer,[9] Yushan Su,[8] Wei Wang,[1,10,†] Xiaonu Xiong,[11] Yi-Bo Yang,[12,13,14,15] Jun Zeng,[1] Jian-Hui Zhang,[16] and Qi-An Zhang[17]

(Lattice Parton Collaboration)

[1]*INPAC, Key Laboratory for Particle Astrophysics and Cosmology (MOE), Shanghai Key Laboratory for Particle Physics and Cosmology, School of Physics and Astronomy, Shanghai Jiao Tong University, Shanghai 200240, China*
[2]*Yang Yuanqing Scientific Computering Center, Tsung-Dao Lee Institute, Shanghai Jiao Tong University, Shanghai 200240, China*
[3]*Faculty of Physics, Adam Mickiewicz University, ulica Uniwersytetu Poznańskiego 2, 61-614 Poznań, Poland*
[4]*Institute of High Energy Physics, CAS, Beijing 100049, China*
[5]*School of Physics, University of Chinese Academy of Sciences, Beijing 100049, China*
[6]*Key Laboratory of Atomic and Subatomic Structure and Quantum Control (MOE), Guangdong Basic Research Center of Excellence for Structure and Fundamental Interactions of Matter, Institute of Quantum Matter, South China Normal University, Guangzhou 510006, China*
[7]*Guangdong-Hong Kong Joint Laboratory of Quantum Matter, Guangdong Provincial Key Laboratory of Nuclear Science, Southern Nuclear Science Computing Center, South China Normal University, Guangzhou 510006, China*
[8]*Department of Physics, University of Maryland, College Park, Maryland 20742, USA*
[9]*Institut für Theoretische Physik, Universität Regensburg, D-93040 Regensburg, Germany*
[10]*Southern Center for Nuclear-Science Theory (SCNT), Institute of Modern Physics, Chinese Academy of Sciences, Huizhou 516000, Guangdong Province, China*
[11]*School of Physics, Central South University, Changsha 418003, China*
[12]*CAS Key Laboratory of Theoretical Physics, Institute of Theoretical Physics, Chinese Academy of Sciences, Beijing 100190, China*
[13]*School of Fundamental Physics and Mathematical Sciences, Hangzhou Institute for Advanced Study, UCAS, Hangzhou 310024, China*
[14]*International Centre for Theoretical Physics Asia-Pacific, Beijing/Hangzhou, China*
[15]*School of Physical Sciences, University of Chinese Academy of Sciences, Beijing 100049, China*
[16]*School of Science and Engineering, The Chinese University of Hong Kong, Shenzhen 518172, China*
[17]*School of Physics, Beihang University, Beijing 102206, China*

(Received 9 December 2024; accepted 28 January 2025; published 20 February 2025)

We calculate the leading-twist light cone distribution amplitudes of the $\Lambda(uds)$ baryon using lattice QCD methods within the framework of large-momentum effective theory. Our numerical computations are carried out with $N_f = 2 + 1$ stout smeared clover fermions and a Symanzik gauge action on a lattice with spacing $a = 0.077$ fm and a pion mass of 303 MeV. To approach the large-momentum region, we simulate the equal-time correlations with the hadron momentum $P^z = \{2.52, 3.02, 3.52\}$ GeV. We investigate the analytic properties of the baryon quasidistribution amplitude in coordinate space and validate them through our lattice calculations. After renormalization and extrapolation, we present results for the three-dimensional distribution in momentum fractions of the two light quarks. Based on these findings, we briefly discuss the phenomenological impact on weak decays of Λ_b and outline potential systematic

*Contact author: junhua@scnu.edu.cn
†Contact author: wei.wang@sjtu.edu.cn

uncertainties that can be improved in the future. This work lays the theoretical foundation for accessing baryon light cone distribution amplitudes from lattice QCD.

DOI: 10.1103/PhysRevD.111.034510

I. INTRODUCTION

Light cone distribution amplitudes (LCDAs) are probability amplitudes for the longitudinal momentum fractions of partons in the leading Fock states of hadrons [1,2]. Within quantum chromodynamics (QCD), the LCDAs play a pivotal role in the description of exclusive processes (e.g., heavy baryon decays) and allow one, e.g., to calculate form factors at asymptotically large-momentum transfer [3,4]. They provide information on hadron structure that is complementary to parton distribution functions. Thus, first-principle calculations of LCDAs benefit not only experimental programs at facilities like the Large Hadron Collider and Jefferson Laboratory, but also testing theoretical mechanisms, e.g., in heavy baryon decays, ultimately deepening our understanding of the strong interactions that govern the behavior of baryons. An example might be the CP violation in heavy baryon decays, with some suggestive clues emerging from recent observations by the LHCb Collaboration [5,6]. Generally speaking, the advent of high-luminosity accelerators has transformed the investigation of exclusive reactions, and thus also of LCDAs, into a highly fertile research field.

In recent decades, significant progress has been made in characterizing the LCDAs of light mesons, including both a few lowest moments [7,8] and the complete x-dependent distribution [9–17]. In contrast, there has been limited advancement in determining baryon LCDAs due to various obstacles. The three valence quarks in a baryon interact with each other through strong forces, leading to a rich and intricate structure that is difficult to describe using simple models. The earliest estimates of the first and second moments of baryon LCDAs were made more than 30 years ago based on the QCD sum rules, known as the Chernyak-Ogloblin-Zhitnitsky model [18]. This result provided a reasonable description of the experimental data at the time and gave a distribution amplitude that deviated significantly from the asymptotic behavior. Meanwhile, advances in perturbation theory have led to a widespread consensus that the analysis of form factors in exclusive processes with large-momentum transfer [19,20] does not indicate a notable deviation of the baryon light cone distribution amplitudes from their asymptotic form [21,22]. Recently, new strategies such as the on-shell wave function method have been proposed, but the results are model dependent [23]. From a phenomenological viewpoint, it has been observed that the $\Lambda_b \to \Lambda$ form factors at large recoil obtained using baryon LCDAs derived from different methods vary significantly [24–26]. This indicates that a reliable and precise result for the baryon LCDA is urgently needed. In addition, a combined analysis of the form factors in this kinematic region and the direct lattice QCD calculation at low recoil [27,28] enables the comprehensive exploration of form factors across the entire kinematic range.

Lattice QCD provides first-principle tools for accessing baryon LCDAs, offering insights into the internal structure of baryons and paving the way for a comprehensive understanding of baryonic systems. Notably, the lowest moments of the leading-twist baryon LCDAs have been computed using operator product expansion (OPE) on the lattice [29,30]. However, in intricate exclusive processes like heavy baryon decay, existing phenomenological analyses do not definitively establish the dominance of the leading-order contributions and therefore require more information than just a few moments. In Refs. [31,32], systematic explorations of the next-to-leading order (NLO) contributions to nucleon form factors have pointed out that the NLO corrections are significant and the nonperturbative evaluation of the entire shape of the baryon LCDAs is necessary.

In recent years, the development of large momentum effective theory (LaMET) [33–35] has presented a promising approach to tackle the light cone distributions. LaMET offers a framework to obtain light cone distributions from equal-time correlation functions in large-momentum hadron states. More explicitly, a connection between these equal-time quasidistribution amplitudes (quasi-DAs) and light cone distribution amplitudes can be established to all orders in QCD perturbation theory. Since LaMET was proposed, it has a wide range of applications, including calculations of quark distribution functions [36–65], gluon distribution functions [66–70], generalized parton distributions [71–82], light cone distribution amplitudes of a light hadron [9–17,83–87] and a heavy meson [88–97], transverse-momentum-dependent distributions [98–119], and double parton distribution functions [120,121]. In contrast with the calculation of a few low moments using the OPE, LaMET enables the extraction of complete x-dependent distribution amplitudes from first principles through lattice computations. These studies of nucleons' parton distribution functions and light mesons' light cone distribution amplitudes have validated the applicability of LaMET.

This paper pioneers lattice QCD computations of baryon LCDAs within the LaMET framework, elucidates the theoretical underpinnings and computational strategies, and presents some numerical results that serve as proof of principle that such calculations are feasible. Future work

will improve the precision and enlarge the scope of such calculations, for example, by analyzing several ensembles and performing a controlled extrapolation to the physical point, thus bridging the gap to a comparison with experimental data.

The subsequent sections of this paper are structured as follows. In Sec. II, we give the theoretical framework including the definitions of LCDA and quasi-DA, renormalization, symmetry properties of quasi-DA, and extrapolations of the results. Section III is dedicated to presenting the numerical outcome from the lattice QCD simulation. Based on these findings, the paper briefly discusses the phenomenological impact on weak decays of Λ_b and identifies potential systematic uncertainties that will be addressed in the future. The final section includes the summary and prospects. Some calculation details are provided in the Appendixes.

II. THEORETICAL FRAMEWORK

In this section, we present the theoretical framework to extract LCDA from equal-time correlation for a fast moving hadron. We start with definitions and explore the renormalization properties of correlations in coordinate space. We further analyze the analytical properties of quasi-DA. We discuss extrapolation of the quasi-DA into regions where direct numerical calculations become difficult. Finally, we present the one-loop matching formula between the quasi- and light cone DAs that are derived in Refs. [84–87].

A. The LCDA and quasi-DA for the Λ baryon

The LCDAs for the Λ baryon are given by the nonlocal hadron-to-vacuum matrix elements at lightlike separations,

$$\begin{aligned} H(z_1,z_2,z_3)_{\alpha\beta\gamma} = \epsilon^{ijk}\langle 0|(W^{ii'}(z_0n,z_1n))u^{i'}_{\alpha}(z_1n) \\ \times (W^{jj'}(z_0n,z_2n))d^{j'}_{\beta}(z_2n) \\ \times (W^{kk'}(z_0n,z_3n))s^{k'}_{\gamma}(z_3n)|\Lambda(P,\lambda)\rangle, \end{aligned} \quad (1)$$

where $|\Lambda(P,\lambda)\rangle$ represents the Λ state with momentum P and helicity λ. $W_{ij}(a,b)$ are lightlike Wilson lines to preserve gauge invariance, and z_0 is an arbitrary reference position on the Wilson lines. The subscripts α,β,γ refer to Dirac indices and the superscripts i, j, k refer to color indices. n is a lightlike vector $n^2=0$ conjugating to the large-momentum P. An illustration of this structure is given in Fig. 1. In the following, to simplify the notation, one can set z_3 (the position of the strange quark) to be zero.

The most general decomposition of the matrix element in Eq. (1) involves 24 invariant functions [122], but only three of them are of leading twist (twist-three),

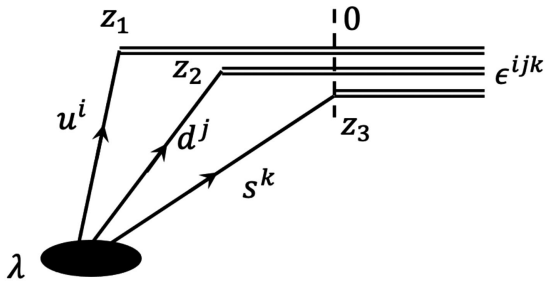

FIG. 1. The structure for the Λ LCDAs, with three Wilson lines connected to the three quarks. z_3 can be set to 0 for simplification.

$$\begin{aligned} H(z_1,z_2,z_3)_{\alpha\beta\gamma} = \frac{1}{4}f_\Lambda\Big[(\not{P}C)_{\alpha\beta}(\gamma_5 u_\Lambda)_\gamma V(z_iP\cdot n) \\ + (\not{P}\gamma_5 C)_{\alpha\beta}(u_\Lambda)_\gamma A(z_iP\cdot n)\Big] \\ + \frac{1}{4}f_\Lambda\Big[(i\sigma_{\mu\nu}P^\nu C)_{\alpha\beta}(\gamma_\mu\gamma_5 u_\Lambda)_\gamma T(z_iP\cdot n)\Big]. \end{aligned} \quad (2)$$

In this equation, f_Λ is the "decay constant" defined by the baryon-to-vacuum matrix element of the local operator,

$$\epsilon_{ijk}\langle 0|u^{i,\mathrm{T}}(0)C\gamma_5\not{n}d^j(0)s^k(0)|\Lambda\rangle = f_\Lambda P^+ u_\Lambda(P). \quad (3)$$

C represents charge conjugation, and u_Λ denotes the Dirac spinor for Λ. $V(z_iP\cdot n)$, $A(z_iP\cdot n)$, and $T(z_iP\cdot n)$ refer to each of the three leading-twist amplitudes, respectively.

By inserting a suitable Dirac matrix Γ, the different leading-twist functions can be projected out,

$$\begin{aligned} \epsilon_{ijk}\langle 0|u^{i,\mathrm{T}}(z_1n)\Gamma d^j(z_2n)s^k(z_3n)|\Lambda\rangle \\ = \Phi(z_1,z_2,\mu)P^+ f_\Lambda u_\Lambda(P), \end{aligned} \quad (4)$$

where μ accounts for the renormalization scale. Therefore, the normalized LCDA as a function of momentum fractions in momentum space can be defined as

$$\begin{aligned} \phi(x_1,x_2,\mu) = \int\frac{P^+dz_1}{2\pi}\int\frac{P^+dz_2}{2\pi}e^{-i(x_1z_1+x_2z_2)P^+} \\ \times\Phi(z_1,z_2,\mu), \end{aligned} \quad (5)$$

where $x_{1,2}$ denote the light cone momentum fractions carried by two light (up and down) quarks. Thereby the momentum fraction of the strange quark is $1-x_1-x_2$. In this work, we only consider the leading-twist component $A(z_iP\cdot n)$ which can be projected out using $\Gamma = C\gamma_5\not{n}$. Reference [30] indicates (based, however, solely on the zeroth and first moments) that A, V, and T are of comparable size, and therefore this study is primarily a proof of principle that such calculations are feasible in LaMET.

In LaMET the LCDAs can be accessed via the lattice simulation of an equal-time matrix element for Λ defined as

$$\tilde{\Phi}_A(z_1,z_2,\mu,P^z)P^z f_\Lambda u_\Lambda(P^z) = \epsilon_{ijk}\langle 0|u^{i,\mathrm{T}}(z_1 n_z)\tilde{\Gamma}d^j(z_2 n_z)s^k(z_3 n_z)|\Lambda(P^z)\rangle. \quad (6)$$

This function is similar to the light cone distribution in Eq. (4), while $n_z = (0,0,0,1)$ is the unit vector along the z direction in Euclidean space. The gauge links are similar and have been omitted here. The Dirac matrix $\tilde{\Gamma} = C\gamma^5\gamma^\nu$ can be chosen as $\nu = t$ or $\nu = z$, both of which could approach the leading-twist projector $C\gamma_5\gamma^+$ on the light cone in the large-momentum limit. In this work, we choose $C\gamma^5\gamma^t$ and call $\tilde{\Phi}_A(z_1,z_2)$ quasi-DA in coordinate space.

The quasi-DA in momentum space can be obtained by a Fourier transformation,

$$\tilde{\phi}_A(x_1,x_2,\mu,P^z) = \int\frac{P^z dz_1}{2\pi}\int\frac{P^z dz_2}{2\pi}e^{-i(x_1 z_1 + x_2 z_2)P^z} \times \tilde{\Phi}_A(z_1,z_2,\mu,P^z). \quad (7)$$

On the lattice, a correlation function is required to extract the quasi-DA, and for the Λ baryon, the appropriate one is defined as

$$C_2(z_1,z_2;t,\vec{P}) = \int d^3x e^{-i\vec{P}\vec{x}}\langle 0|\hat{O}_\gamma(\vec{x},t;z_1,z_2) \times \bar{\hat{O}}_{\gamma'}(0,0;0,0)T^{\gamma\gamma'}|0\rangle, \quad (8)$$

where T represents the projection operator used to extract matrix components from correlation functions; it is selected as $(I+\gamma^t)/2$ for the Λ baryon with $I(J^P) = 0(\frac{1}{2}^+)$. The baryonic operator $\hat{O}_\gamma(\vec{x},t;z_1,z_2)$ consists of three quark fields and three Wilson lines,

$$\hat{O}_\gamma(\vec{x},t;z_1,z_2) = \epsilon^{ijk}W^{ii'}(z_0,\vec{x}+z_1 n_z)u^{i'}_\alpha(\vec{x}+z_1 n_z,t) \times \tilde{\Gamma}_{\alpha\beta}W^{jj'}(z_0,\vec{x}+z_2 n_z,t)d^{j'}_\beta(\vec{x}+z_2 n_z) \times W^{kk'}(z_0,\vec{x})s^{k'}_\gamma(\vec{x},t), \quad (9)$$

where $W(z_0,\vec{x})$ denotes the Wilson line in coordinate space. For simplicity, we have set z_3 to zero. The reference position z_0 of Wilson lines in $\hat{O}_\gamma(\vec{x},t;z_1,z_2)$ is arbitrary, and for simplicity, we set it to the same value as that of the strange quark. Therefore, the operator can be expressed as

$$\hat{O}_\gamma(\vec{x},t;z_1,z_2) = \epsilon^{ijk}W^{ii'}(\vec{x},\vec{x}+z_1 n_z)u^{i'}_\alpha(\vec{x}+z_1 n_z,t) \times \tilde{\Gamma}_{\alpha\beta}W^{jj'}(\vec{x},\vec{x}+z_2 n_z)d^{j'}_\beta(\vec{x}+z_2 n_z,t) \times s^k_\gamma(\vec{x},t), \quad (10)$$

which contains only on two Wilson lines.

B. Renormalization

The nonlocal operator in correlation functions includes Wilson lines that contain both linear and logarithmic ultraviolet divergences. Nonperturbative renormalization schemes are required to remove these divergences. Over the past years, several renormalization schemes have been proposed to eliminate these divergences, including Wilson line renormalization [9,123], regularization-independent momentum subtraction (RI/MOM) renormalization [11,124], hybrid renormalization [14,125], and self-renormalization [15,126].

The RI/MOM renormalization scheme has been extensively used in the renormalization of local operators, but its application to nonlocal operators is a topic of ongoing debate. Recent studies [127] indicate that the RI/MOM scheme depends on the accuracy of gauge fixing. With precise gauge fixing, the outcomes in the RI/MOM scheme align with perturbative results at short distances. However, for large distances, the RI/MOM scheme still introduces artificial infrared effects.

The hybrid renormalization approach [125] provides a novel strategy by implementing different renormalization schemes in distinct coordinate regions and thereby offers a promising framework for addressing the renormalization of nonlocal operators. In this framework, self-renormalization [126] can be utilized at long distances by comparing large-momentum matrix elements with zero-momentum matrix elements. This entails extracting linear divergences and other parameters from zero-momentum matrix elements with different lattice spacings, which can be applied to renormalize the large-momentum matrix elements without introducing additional infrared contributions. At short distances, a ratio of the matrix elements with large and zero momentum can be taken and then matched to the perturbative result. This also removes additional artifacts at small spatial separations.

The hybrid scheme with self-renormalization becomes the mainstream scheme for studying LCDAs with LaMET [15–17]. Some theoretical details of hybrid renormalization for light baryons have already been presented in Refs. [85,87], however, the numerical realization is quite involved. First, to extract the linear divergence, multiple zero-momentum matrix elements at different lattice spacings need to be calculated on the lattice. Second, this scheme requires a perturbative matching at short distance to extract the renormalization factors. According to [85], the perturbative zero-momentum matrix element of Λ is

$$\hat{M}_p(z_1,z_2,\mu,,P^z=0) = 1+\frac{\alpha_s C_F}{2\pi}\left[\frac{7}{8}\ln\left(\frac{z_1^2\mu^2 e^{2\gamma_E}}{4}\right) + \frac{7}{8}\ln\left(\frac{z_2^2\mu^2 e^{2\gamma_E}}{4}\right) + \frac{3}{4}\ln\left(\frac{(z_1-z_2)^2\mu^2 e^{2\gamma_E}}{4}\right) + 4\right]. \quad (11)$$

In the above equation, $\hat{M}_p(z_1, z_2, \mu, P^z = 0)$ is a zero-momentum quasidistribution in the $\overline{\text{MS}}$ scheme, which at short distance can be identified as the renormalized quasi-distribution $\tilde{\Phi}_A(z_1, z_2, \mu, P^z = 0)$. μ is the renormalization scale and we use $\mu = 2$ GeV. The typical distance to ensure the perturbative matching is $z < 0.3$ fm. Third, it is crucial to observe from the aforementioned equation that divergences occur at $z_1 = 0$, $z_2 = 0$, and $z_1 = z_2$, necessitating that numerical matching steers clear of lattice results in close proximity to these divergences. Consequently, this constraint restricts the availability of valuable data for finite lattice spacings. Therefore, the implementation of hybrid renormalization mandates extremely small lattice spacings and accurate computations of correlation functions.

Therefore, in this preliminary study, we use the ratio of large- to zero-momentum matrix elements for renormalization, bearing in mind that the systematic errors are introduced by spurious infrared physics at long distances. The renormalized quasi-DA can then be expressed as

$$\tilde{\Phi}_A(z_1, z_2, \mu, P^z \neq 0) = \frac{\tilde{\Phi}^0_A(z_1, z_2, \mu, P^z \neq 0)}{\tilde{\Phi}^0_A(z_1, z_2, \mu, P^z = 0)}. \tag{12}$$

C. Analytic properties of quasi-DA

Before initiating numerical simulations, we can leverage certain analytic properties to streamline our calculations.

To discuss the analytical properties of $\tilde{\Phi}(z_1, z_2)$, we distinguish eight regions, as shown in Fig. 2, and use two symmetries to simplify the calculation.

(i) The isospin symmetry originates from the fact that lattice simulations do not distinguish u and d masses in the clover action adopted in our simulation. As z_1 and z_2 are the coordinates of the u and d quarks, we have the equality

$$\tilde{\Phi}(z_1, z_2) = \tilde{\Phi}(z_2, z_1). \tag{13}$$

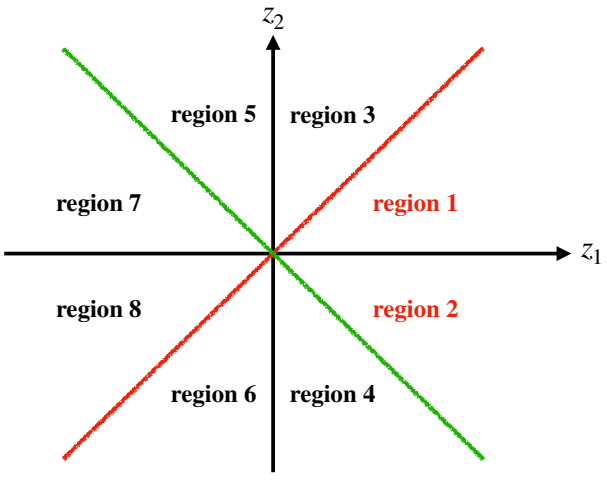

FIG. 2. Eight regions in z_1-z_2 plane.

(ii) Another constraint arises from the fact that the LCDA and the quasi-DA in momentum space are real,

$$\tilde{\phi}(z_1, z_2, \mu) = \int_0^1 dx_1 \int_0^1 dx_2 e^{i(x_1 z_1 P^z + x_2 z_2 P^z)} \times \tilde{\Phi}(x_1, x_2, \mu), \tag{14}$$

the real part of the quasi-DA in coordinate space is symmetric, and the imaginary part is antisymmetric. Then $\tilde{\Phi}(z_1, z_2)$ satisfies

$$\tilde{\Phi}(z_1, z_2) = \tilde{\Phi}^*(-z_1, -z_2). \tag{15}$$

Therefore, the symmetry of the eight regions in Fig. 4 can be summarized as follows:

$$\begin{aligned} &\tilde{\Phi}_1(z_1, z_2) = \tilde{\Phi}_3(z_2, z_1) = \tilde{\Phi}^*_6(-z_2, -z_1) = \tilde{\Phi}^*_8(-z_1, -z_2), \\ &\tilde{\Phi}_2(z_1, z_2) = \tilde{\Phi}^*_4(-z_2, -z_1) = \tilde{\Phi}_5(z_2, z_1) = \tilde{\Phi}^*_7(-z_1, -z_2). \end{aligned} \tag{16}$$

Based on these symmetries, only regions 1 and 2 are independent. Given that the propagators for the u and d quarks are identical in our lattice simulation, the first symmetry holds true for each configuration. The second symmetry stems from the physical constraints imposed on the quasi-DA in momentum space; such symmetry is only revealed after averaging lattice data over configurations. Consequently, data from regions 4 and 6 can also be generated on the lattice and subsequently merged with data from regions 1 and 2 to enhance statistical significance. Furthermore, as a result of these symmetries along the diagonal line where $z_1 = -z_2$, represented by the green line in Fig. 2, it holds that $\text{Im}[\tilde{\Phi}(z_1, z_2)] \equiv 0$.

D. Extrapolation

Numerical uncertainties for quasi-light-front correlations increase rapidly with growing spatial separations, and a brute-force truncation of the Fourier transformation can lead to unphysical oscillations in momentum space. Hence, in conjunction with the hybrid scheme, physically motivated extrapolations for long distances have been recommended [125]. A model based on the asymptotic behavior of the light baryon LCDAs in momentum space is given as

$$\phi(x_1, x_2) = C_0 x_1^{d_1} x_2^{d_1} (1 - x_1 - x_2)^{d_2}, \tag{17}$$

where C_0 is a normalization factor, and $d_{1,2}$ are undetermined exponents.

Generally, for parton distribution functions (PDFs) or meson LCDAs, we can perform an analytical Fourier transform of the asymptotic behavior and take the limit

of large light front distance to obtain the extrapolation form in coordinate space. However, for baryon LCDAs, the analytical Fourier transform becomes complicated and, similar to perturbative expressions in self-renormalization, encounters divergency issues at short distances. In this work, we adopt a simplified approach: take the numerical Fourier transformation from Eq. (17) and then perform the fitting for quasi-DA in coordinate space,

$$\tilde{\Phi}(z_1,z_2;d_1,d_2)=\int_0^1 dx_1\int_0^1 dx_2\, e^{ix_1z_1P^z}e^{ix_2z_2P^z}\times C_0x_1^{d_1}x_2^{d_1}(1-x_1-x_2)^{d_2}. \tag{18}$$

This form is applied only when z_1 and z_2 are large, hence we utilize it only in the coordinate-space regions marked in red and blue in Fig. 4.

There is an asymmetry between the red and blue regions in the first and fourth quadrants in Fig. 4. This asymmetry is a result of the nonsymmetrical distribution in the z_1-z_2 plane, which has implications for our extrapolation process. Based on the definition of the baryon quasi-DA and prior analytic discussions, we use two Wilson lines, $W^{ii'}(\vec{x},\vec{x}+z_1n_z)$ and $W^{jj'}(\vec{x},\vec{x}+z_2n_z)$, which link the u and d quark fields to s in coordinate space. These two Wilson lines can be oriented either in the same direction or in opposite directions, which have different consequences:

(i) As illustrated in Fig. 2, the Wilson lines point in opposite directions in the second and fourth quadrants, as depicted in the right panel of Fig. 3. Consequently, in such scenarios, the effective Wilson length can be simply obtained as $|z_1|+|z_2|$.

(ii) In the first and third quadrants, as shown in the left panel of Fig. 3, when z_1 and z_2 point in the same direction, one can demonstrate

$$\begin{aligned}&W(z_1,0)^{i'i}W(z_2,0)^{j'j}\epsilon^{ijk}\\&\quad=W(z_1,z_2)^{i'i''}W(z_2,0)^{i''i}W(z_2,0)^{j'j}\epsilon^{ijk}\\&\quad=W(z_1,z_2)^{i'i''}W^{\dagger}(z_2,0)^{kk'}\epsilon^{i''j'k'}.\end{aligned} \tag{19}$$

Therefore, in this scenario, the effective length of the Wilson lines is given by $\max(|z_1|,|z_2|)$.

Hence, the effective length of the Wilson lines is larger in the second and fourth quadrants than in the first and third quadrants. This implies that the uncertainty is more significant in the second and fourth quadrants than in the first and third quadrants for the same $|z_1|$ and $|z_2|$. Additionally, the magnitude of the quasi-DA will decay more rapidly in the second and fourth quadrants. Consequently, a good signal area will resemble a diamond shape, as illustrated by the orange line in Fig. 4.

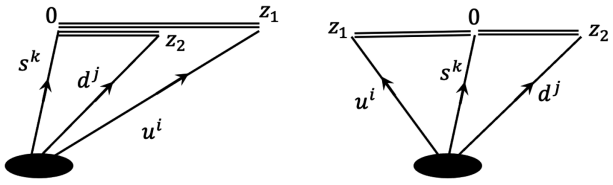

FIG. 3. The Wilson lines for two cases of z_1 and z_2. The left and right panels correspond to the fact that the two gauge links are parallel and antiparallel, respectively.

Considering the symmetries described in Eq. (16), it is sufficient to extrapolate the triangular regions 1 and 2, as illustrated in Fig. 2. By combining these symmetries with the Wilson line properties discussed in the previous paragraph, we can now elaborate on the extrapolation regions outlined in Fig. 4.

(i) On the axis $z_1=-z_2$, represented by the green blocks in Fig. 4, the imaginary components of the quasi-DA are constrained to be zero. Therefore, only the real part of $\Phi(z_1,z_2)$ within the green blocks contributes to the extrapolation process.

(ii) The red blocks mark the regions where $z_1\gg 0$ and $z_2\gg 0$. In these regions, both z_1 and z_2 need to be extrapolated. However, when the lengths are equal, i.e., $|z_1|=|z_2|$, the effective Wilson line length is significantly larger in region 2 compared to region 1. Consequently, the red blocks in region 2 initiate from a smaller $|z_{1,2}|$. In contrast, the blue blocks denote scenarios with a finite z_2 while $z_1\gg 0$, and only z_1 requires extrapolation in this context. Similarly, due to the varying effective Wilson line lengths in regions 1 and 2, the shapes of the blue blocks will differ between the two regions.

E. Two-dimensional matching

In LaMET, the quasidistributions can be factorized into perturbative matching kernels convoluted with light cone distributions. For the baryon LCDA involving two momentum fractions, this factorization takes the form

$$\tilde{\phi}(x_1,x_2)=\int_0^1 dy_1\int_0^{1-y_1} dy_2 C(x_1,x_2,y_1,y_2)\phi(y_1,y_2)+\mathcal{O}\left(\frac{\Lambda^2_{\rm QCD}}{(x_1P^z)^2},\frac{\Lambda^2_{\rm QCD}}{(x_2P^z)^2},\frac{\Lambda^2_{\rm QCD}}{[(1-x_1-x_2)P^z]^2}\right). \tag{20}$$

Here $\tilde{\phi}(x_1,x_2)$ represents the quasi-DA in momentum space, and $\phi(x_1,x_2)$ represents the LCDAs. The power correction terms $\Lambda^2_{\rm QCD}/(x_1P^z)^2$, $\Lambda^2_{\rm QCD}/(x_2P^z)^2$, and $\Lambda^2_{\rm QCD}/[(1-x_1-x_2)P^z]^2$ are suppressed in the large-momentum limit. The matching kernel can be expressed through a perturbative expansion as

$$C(x_1,x_2,y_1,y_2)=\delta(x_1-y_1)\delta(x_2-y_2)+\frac{\alpha_sC_F}{2\pi}c^{(1)}(x_1,x_2,y_1,y_2)+\mathcal{O}(\alpha_s^2). \tag{21}$$

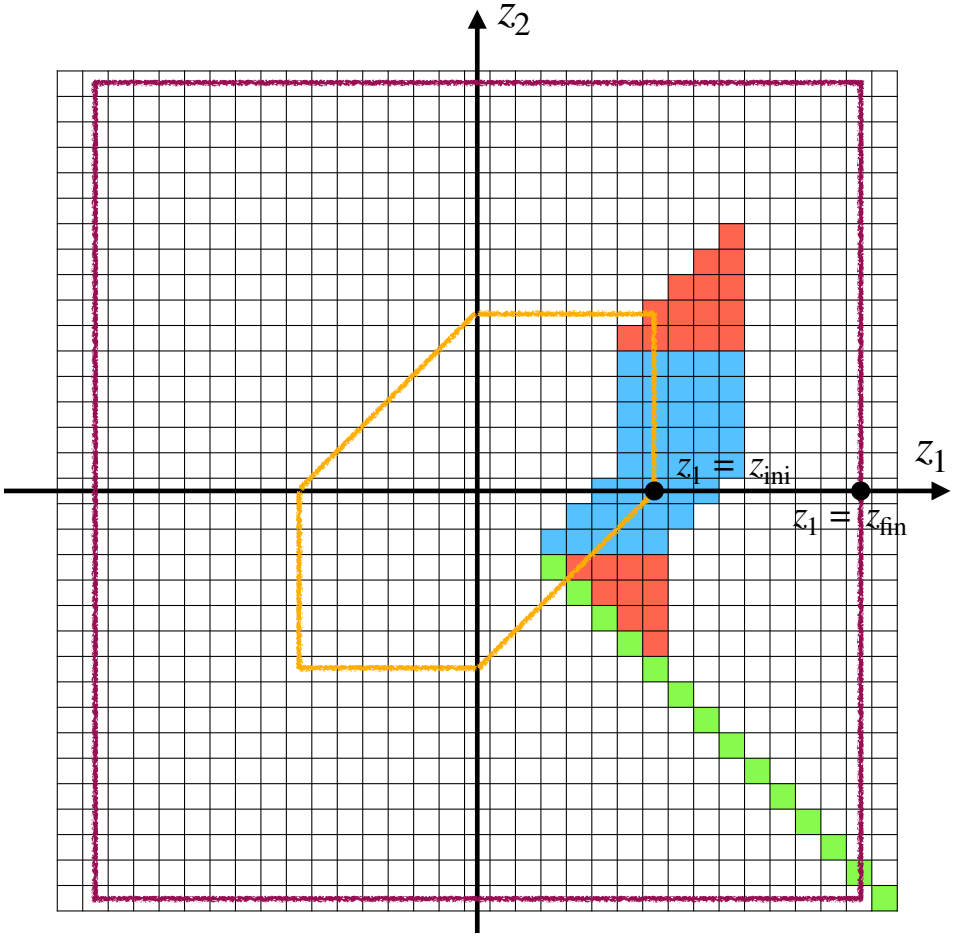

FIG. 4. The extrapolation regions in the z_1-z_2 plane. Each grid represents one lattice spacing. Raw data with good signal/noise were obtained for the rhombus indicated by the orange line. Extrapolations are based on these data. The meaning of the different color blocks is discussed in the main text. $z_{\rm ini}$ and $z_{\rm fin}$ indicate the region for which the quasi-DA was extrapolated.

The detailed expressions for $c^{(1)}(x_1, x_2, y_1, y_2)$ in terms of the "double-plus function" $f_\oplus$ are compiled in Appendix A.

Two numerical methods are commonly used for implementing the matching:

(i) numerically discretizing the matching kernel and performing its inversion; and
(ii) iteratively performing the matching by expanding higher-order terms in the kernel.

In the matching process, the matching kernel is represented as a four-dimensional tensor. Although it is possible to reduce this tensor to two dimensions utilizing the properties of the double-plus function and subsequently carrying out a numerical inversion, we introduce an iterative approach in this work to facilitate a more straightforward numerical implementation.

The dominant term in the matching kernel, as given by Eq. (21), is a Dirac δ function. The discrepancy between ϕ and $\tilde{\phi}$ is of order α_s at the one-loop level. Thus, by substituting Eq. (21) into Eq. (20), we obtain

$$\phi(x_1, x_2) = \tilde{\phi}(x_1, x_2) - \frac{\alpha_s C_F}{2\pi} \int_{-\infty}^{\infty} dy_1 \int_{-\infty}^{\infty} dy_2 \times c^{(1)}(x_1, x_2, y_1, y_2)\tilde{\phi}(y_1, y_2) + \mathcal{O}(\alpha_s^2). \quad (22)$$

In this equation, we extend the integration limits of (0, 1) and $(0, 1-y)$ to $(-\infty, \infty)$; such extension may introduce systematic uncertainties at higher orders. The subsequent leading-order matching kernel $c^{(1)}(x_1, x_2, y_1, y_2)$ is a double-plus function involving the variables x_1 and x_2,

$$\begin{aligned} c^{(1)}(x_1, x_2, y_1, y_2) &= [f(x_1, x_2, y_1, y_2)]_\oplus \\ &= f(x_1, x_2, y_1, y_2) - \delta(x_1 - y_1)\delta(x_2 - y_2) \\ &\times \int_{-\infty}^{\infty} dt_1 \int_{-\infty}^{\infty} dt_2 f(t_1, t_2, y_1, y_2). \end{aligned} \quad (23)$$

By substituting Eq. (23) into Eq. (22), these singularities in $f(x_1, x_2, y_1, y_2)$ can be canceled between the first and

second term in Eq. (23) with the constraints $x_1 = y_1$ and $x_2 = y_2$. Then the matching equation simplifies to

$$\phi(x_1,x_2) = \tilde{\phi}(x_1,x_2) - \frac{\alpha_s C_F}{2\pi}\left[\int dy_1 dy_2 [f(x_1,x_2,y_1,y_2) \times \tilde{\phi}(y_1,y_2) - f(y_1,y_2,x_1,x_2)\tilde{\phi}(x_1,x_2)]\right], \quad (24)$$

which is free of any plus function.

Recent studies have explored matching kernels in different renormalization schemes for the baryon LCDA. The $\overline{\text{MS}}$ bar scheme and RI/MOM scheme matching kernels for the leading-twist function $A(z_i P\cdot n)$ are presented in [84]. The hybrid scheme matching kernels for $V(z_i P\cdot n)$, $A(z_i P\cdot n)$, and $T(z_i P\cdot n)$ functions combining self-renormalization and ratio scheme renormalization have been collected in [85,87]. Furthermore, the matching kernels in coordinate space in the ratio scheme for the three leading-twist distributions are displayed in [86]. From all of them, the ratio scheme matching kernel is adopted in this work. For further details and discussions on the matching kernel, please refer to the Appendix A.

III. NUMERICAL RESULTS

A. Lattice setup

The configurations used in this study are based on the stout smeared clover fermion action coupled with Symanzik gauge action, under periodic boundary conditions, generated by the CLQCD Collaboration [128]. These configurations have been successfully applied in studies involving hadron spectrum [129–131], decay and mixing of charmed hadrons [132–136], heavy meson LCDAs [94,97], PDFs of a deuteronlike dibaryon [63], and other interesting observables [137,138]. We here use a single ensemble, F32P30, characterized by a lattice spacing of $a = 0.07746(18)$ fm and a volume of $n_s^3 \times n_t = 32^3 \times 96$. The valence light quark mass is set to match the sea quark mass, with $m_\pi = 303.2(1.3)$ MeV. To explore the momentum dependence of the Λ LCDA and approach the infinite momentum limit, we consider three different hadron momenta: $P^z = \{5,6,7\} \times 2\pi/(n_s a) = \{2.52, 3.02, 3.52\}$ GeV. In numerical simulations, we use point sources with momentum smearing [139] and APE smearing [140]. These techniques significantly improve the signal-to-noise ratio for the large P_z case. Parameters in momentum smearing are chosen as $p = 3$ with the smearing size and iteration number $\{5, 50\}$. Overall, our simulation comprises 777 configurations, with 9×6 source positions on each configuration, leading to a total of $777 \times 9 \times 6$ measurements.

B. Dispersion relation

Before analyzing the quasi-DAs and LCDAs, we first give the dispersion relation for the Λ baryon, which can be used as a test of our setup and as a check of our two-point function results.

To analyze the dispersion relation, we evaluate the local two-point correlation function $C_2(0,0;t,P^z)$, as defined in Eq. (8), across a range of hadron momenta from 0 to 3.52 GeV. The effective energy is extracted by fitting the parametrization $C_2(0,0;\tau,P^z) = c_0 e^{-E_0\tau}(1 + c_1 e^{-\Delta E\tau})$ for Euclidean time $\tau = it$. In this expression, the E_0 corresponds to the total energy of the hadron with P^z.

To quantify the discretization effects in the relationship between the effective energy and hadron momentum, we utilize the following fitting ansatz:

$$E^2 = m_\Lambda^2 + c_2 (P^z)^2 + c_3 (P^z)^4, \quad (25)$$

where the parameters c_2 and c_3 are chosen to quantify the deviation from the continuum limit, $E^2 = m_\Lambda^2 + (P^z)^2$. The fitted values obtained, as depicted in Fig. 5, are $c_2 = 1.058(44)$ and $c_3 = -0.0152(66)$, which are in proximity to 1 and 0, respectively. Hence, a slight deviation is observed between the lattice outcome and the continuum prediction, which may imply that the discretization errors are less significant. We defer a full analysis of discretization effects to future work.

C. Extraction of quasi-DAs

In lattice simulations, the nonlocal two-point correlation function $C_2(z_1,z_2;t,P^z)$ is utilized to determine the matrix element of equal time, as defined in Eq. (6), including the contribution from the ground state. To extract the ground-state matrix element, which represents the

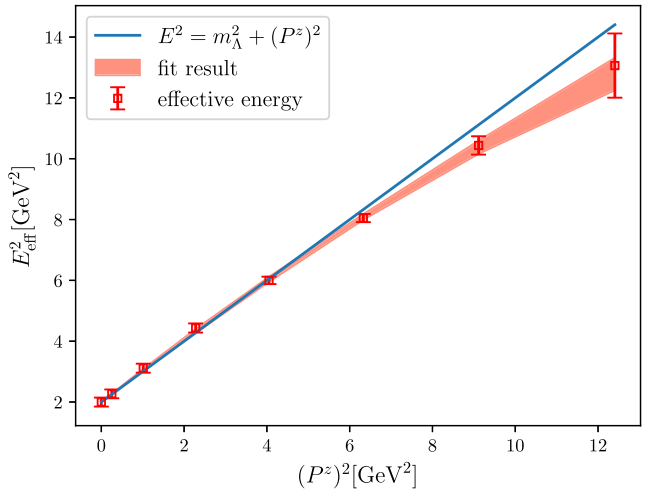

FIG. 5. Dispersion relation for the Λ baryon on the ensemble F32P30.

quasi-DA, we analyze the renormalized two-point function $C_2^{\mathrm{rn}}(z_1, z_2; t, P^z)$

$$C_2^{\mathrm{rn}}(z_1,z_2;t,P^z) = \frac{C_2(z_1,z_2;t,P^z)C_2(0,0;t,0)}{C_2(z_1,z_2;t,0)C_2(0,0;t,P^z)} = \tilde{\Phi}(z_1,z_2,P^z)\frac{1+c_0(z,P^z)e^{-\Delta E\tau}}{1+c_1(z,P^z)e^{-\Delta E\tau}}. \quad (26)$$

Here τ represents the Euclidean time, with c_0, c_1, and ΔE serving as parameters that account for excited-state contamination. As τ becomes sufficiently large, the term $e^{-\Delta E\tau}$ significantly suppresses the contribution from excited states, thereby justifying a one-state fit at large τ. To compare the effectiveness of one- and two-state fits, we conduct an analysis at a specific instance of z_1, z_2, as shown in Fig. 6. The results indicate that the one-state fit provides a clear interpretation of the data, consistent with the two-state fit. Normally, the one-state fit provides a greater robustness across different values of z_1, z_2, and P^z compared to the two-state fit. As a result, we will utilize the one-state fit for subsequent analyses.

The renormalized quasi-DA of a baryon depends on both z_1 and z_2. To elucidate the behavior of the quasi-DA as the nonlocal separation increases, we present $\tilde{\Phi}(z_1, z_2)$ in Fig. 7 and investigate the variation with z_2 for fixed z_1 at several specific values. When $z_1 = 0a$, the real and imaginary parts of $\tilde{\Phi}(z_1, z_2)$ exhibit axial and central symmetry at axis $z_2 = 0$ and point $z_1 = z_2 = 0$, respectively. However, this symmetry diminishes as z_1 increases. Further examples of $\tilde{\Phi}(z_1, z_2)$ with fixed z_1 are discussed in Appendix B, showing similar trends. Moreover, the data indicate slightly larger uncertainties in the region $z_2 < 0$ compared to $z_2 > 0$ when $z_1 > 0$, which can be attributed

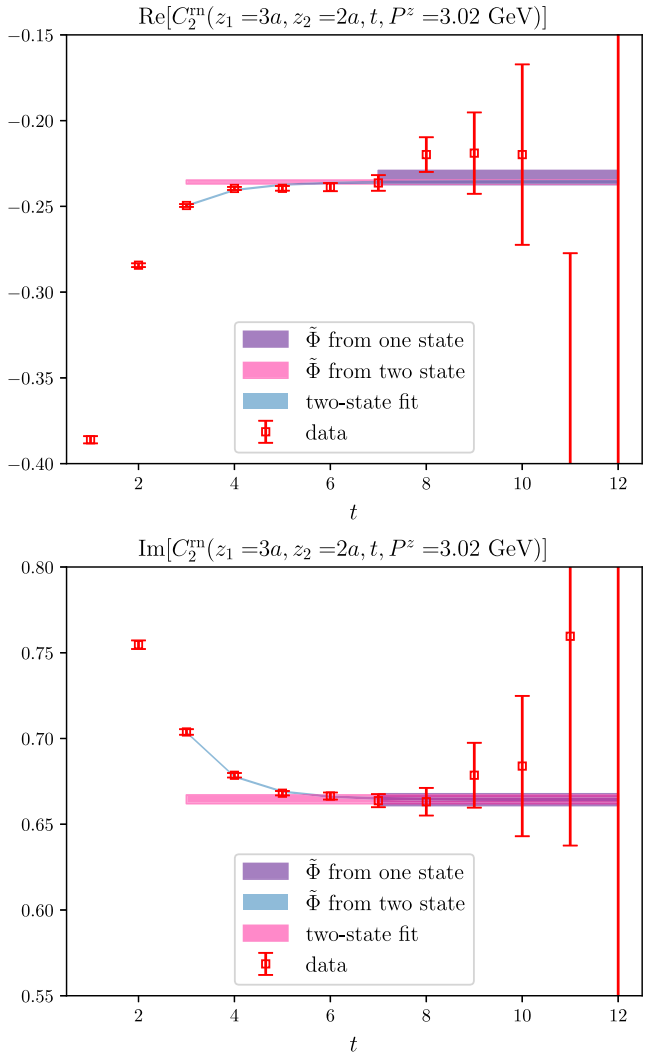

FIG. 6. Comparison of one- and two- state fit for the renormalized nonlocal two-point function. The upper and lower panels show the real and imaginary parts of $C_2^{\mathrm{rn}}(z_1, z_2, t, P^z)$ at $\{z_1, z_2, P^z\} = \{3a, 2a, 3.02\ \mathrm{GeV}\}$. In each panel, the colored bands for $\tilde{\Phi}$ represent the plateaus and the fit ranges.

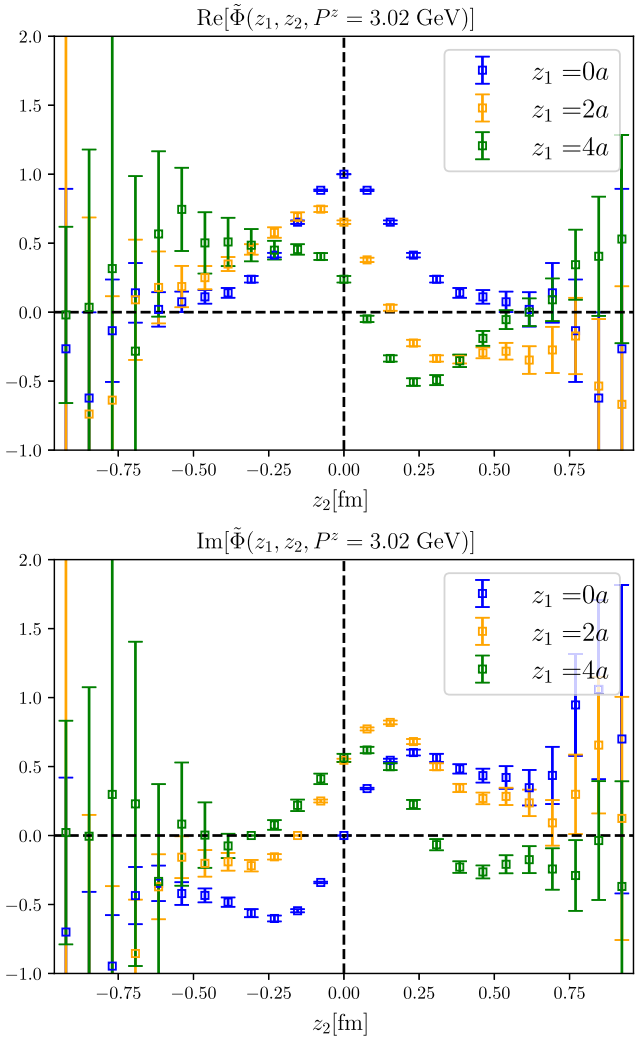

FIG. 7. The figures correspond to Re[$\tilde{\Phi}(z_1, z_2)$] (upper) and Im[$\tilde{\Phi}(z_1, z_2)$] (lower) with fixed z_1 at $P^z = 3.02$ GeV.

to the orientation of the Wilson lines for $z_{1,2}$ being either parallel or antiparallel, as depicted in Fig. 3. Additionally, the uncertainties notably increase at larger z_2 values due to the extended Wilson lines in nonlocal operators. This highlights the necessity of performing an extrapolation in both z_1 and z_2 to accurately capture the long-distance information, as elaborated in Sec. II D.

Figure 8 presents a three-dimensional visualization of the central value of the renormalized quasi-DA in coordinate space, $\tilde{\Phi}(z_1, z_2)$. However, due to substantial uncertainties in the large z_1 and z_2 region, only data in the central region are displayed.

In this figure, the data behavior aligns with the analytical expectations outlined in our framework:

(i) Both the real and imaginary parts exhibit pronounced oscillations along $z_1 = z_2$, with amplitudes decaying slowly. This observation validates the expectation derived from the perturbative calculation discussed near Eq. (11).

(ii) The imaginary part consistently approaches zero along $z_1 = -z_2$, in accordance with the analytic properties dictated by the two symmetries.

(iii) The areas with good signals resemble a diamond shape, as illustrated in Fig. 9 through the heat map of relative uncertainty. This pattern reflects the effective length for two Wilson lines with parallel in the antiparallel direction, as detailed in Sec. II D.

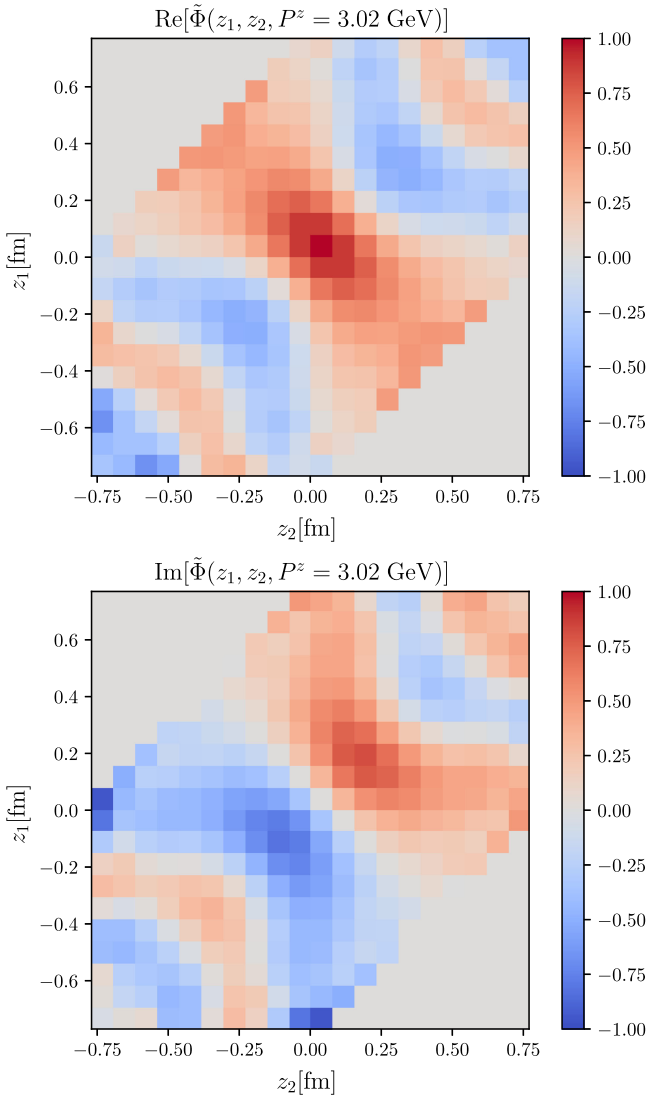

FIG. 8. The central value of $\tilde{\Phi}(z_1, z_2)$ in the z_1-z_2 plane is displayed in the figures, including the real (upper) and imaginary (lower) part. The color density represents the value.

D. Numerical extrapolation

Performing a Fourier transformation with limited data points in coordinate space will induce unphysical oscillations, as discussed in Sec. II D, and have been highlighted in previous studies [14,15,108,111,113]. To eliminate these effects, we employ extrapolation techniques. According to Eq. (18), we conduct a two-parameter fit for d_1 and d_2 applied to the renormalized matrix elements $\tilde{\Phi}(z_1, z_2, \mu, P^z)$, with the fitting region shown in Fig. 4. As explained in Fig. 4, the data points are grouped into red and blue blocks for the fit procedure, corresponding to $\{z_1 \gg 0, z_2 \gg 0\}$ and a finite z_2 with $z_1 \gg 0$, respectively.

First, we examine the extrapolation results within the designated regions to assess the effectiveness of the fit function (18) in both the blue and the red regions as illustrated in Fig. 4. The different results for the fitting parameters d_1 and d_2 are compiled in Table I. These findings reveal that the values of d_1 and d_2 from analyses that include both regions, as well as those exclusively from the red region, are consistent within at most 2 standard deviations. This consistency demonstrates that the

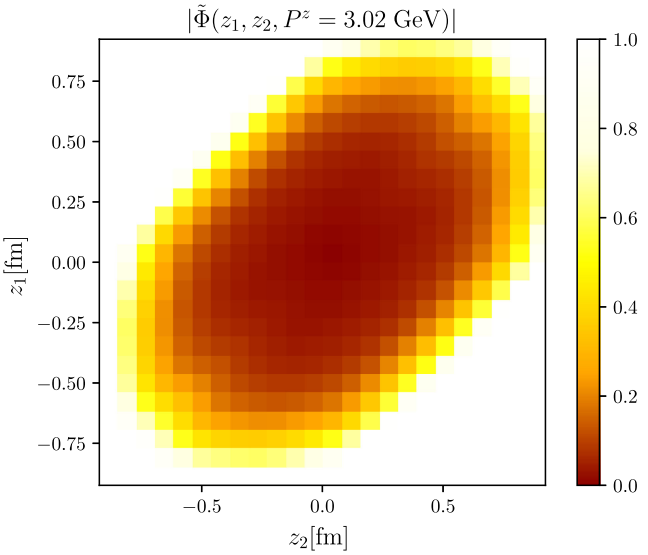

FIG. 9. The uncertainties of $|\tilde{\Phi}(z_1, z_2)|$ in the z_1-z_2 plane. A deeper color indicates a smaller uncertainty.

TABLE I. Fit parameters d_1 and d_2 obtained for the three hadron momenta $P^z = \{2.58, 3.02, 3.52\}$ GeV and utilizing in each case the data from either the red or the red and blue region in Fig. 4.

Momenta (GeV)	d_1, d_2 from red region	d_1, d_2 from red and blue regions
$P^z = 2.52$	0.042(40), 0.377(62)	0.101(25), 0.459(39)
$P^z = 3.02$	0.049(45), 0.545(85)	0.046(21), 0.480(45)
$P^z = 3.52$	0.072(55), 0.546(67)	0.021(12), 0.449(30)

inclusion of the blue region exerts a minor influence. Consequently, we incorporate both the red and blue regions for extrapolation in the following analysis.

Second, to mitigate the systematic effects due to our choice of fitting regions, we determine d_1 and d_2 for several slightly shifted fitting regions. The "standard" region encompasses the areas marked as red or blue in Fig. 4. In addition, three other scenarios are analyzed in which this region is either shifted forward by one lattice unit in the $+z_1$ or $-z_1$ direction or by two units in the $+z_1$ direction. The maximal differences for d_1 and d_2 are treated as systematic error. Table II summarizes the result including systematic error.

Note that the central value of d_1 is smaller than that of d_2, and both are considerably smaller than unity. This discrepancy might lead to a mild convergence for $\tilde{\Phi}(z_1, z_2)$ as z_1 and z_2 increase. Therefore, the end point behavior with x_1, $x_2 \to 0$ in momentum space might also be affected. This situation could be improved in the future by performing a more precise calculation with larger statistics on a fine lattice.

Finally, the extrapolated data are displayed in Fig. 10, where the upper panel illustrates the behavior of Re $[\tilde{\Phi}(z_1, z_2)]$ in the red blocks shown in Fig. 4, and the lower panel corresponds to the blue blocks. As discussed in Sec. II D, the asymptotic behavior is applicable when z_1 and z_2 are large. In this analysis, the data included in the fitting predominantly fall within $\lambda \sim [5, 10]$. Within this region, the extrapolated band aligns well with the original data, thereby validating the effectiveness of applying this asymptotic behavior, though more systematic uncertainties should be taken into account in the future.

As a result, we incorporate extrapolated data ranging from z_{ini} to z_{fin}, as depicted in Fig. 4. The regions within the gray lines are populated with lattice data, while the areas between the gray and blue lines are supplemented with data

TABLE II. Final results for the fitting parameters d_1 and d_2.

Momenta (GeV)	d_1	d_2
$P^z = 2.52$	0.118(68)	0.50(22)
$P^z = 3.02$	0.052(34)	0.49(18)
$P^z = 3.52$	0.13(12)	0.63(21)

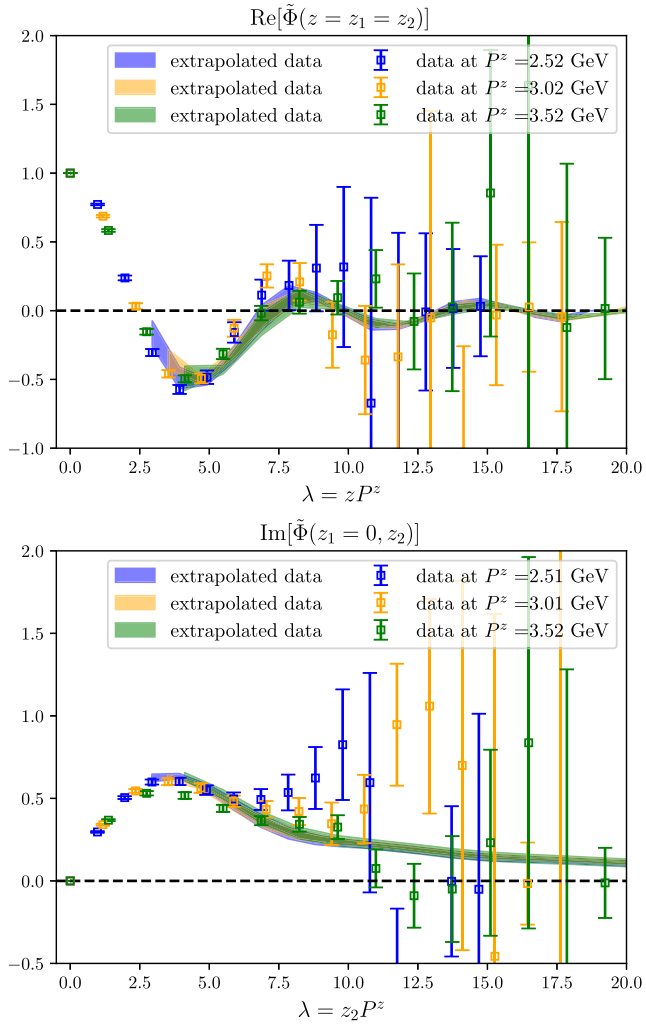

FIG. 10. Two examples of extrapolation for the renormalized matrix elements $\tilde{\Phi}(z_1, z_2, P^z)$ as functions of z_1, z_2. Upper: corresponds to Re$[\tilde{\Psi}(\lambda = z_2P^z)]$ when $z_1 = z_2$. Lower: represents Im$[\tilde{\Psi}(\lambda = z_2P^z)]$ at $z_1 = 0$. The results of three hadron momenta are all displayed. The fit region in each plot is approximately within $\lambda \sim [5, 10]$, not all areas of colored bands.

derived from extrapolation. This approach is justified as $\tilde{\Psi}(z_1, z_2)$ exhibits a clear signal within the inner hexagon region.

E. Quasi-DA in momentum space

The quasi-DA in momentum space $\tilde{\phi}(x_1, x_2, \mu, P^z)$ can be derived from the extrapolated quasi-DA in coordinate space $\tilde{\Phi}(z_1, z_2, \mu, P^z)$ by the Fourier transformation in Eq. (7). We display the result in Fig. 11, where $\tilde{\phi}(x_1, x_2)$ is shown for $P^z = 3.02$ GeV and $x_1 = \{0.25, 0.5, 0.75\}$ as function of x_2.

Since x_1 and x_2 are the momentum fractions of u and d quarks, respectively, both of them are predominantly quite small, implying that the strange quark momentum fraction is quite large. This distribution can be partially

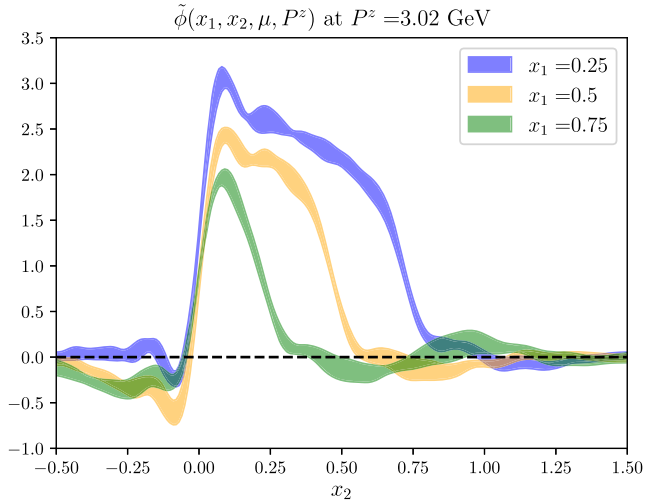

FIG. 11. The quasi-DA $\tilde{\phi}(x_1, x_2, \mu, P^z)$ in momentum space as a function of x_2 at $x_1 = \{0.25, 0.5, 0.75\}$ with hadron momentum $P^z = 3.02$ GeV. Because $\tilde{\phi}(x_1, x_2, \mu, P^z)$ is real by definition, only the real part is shown in this figure.

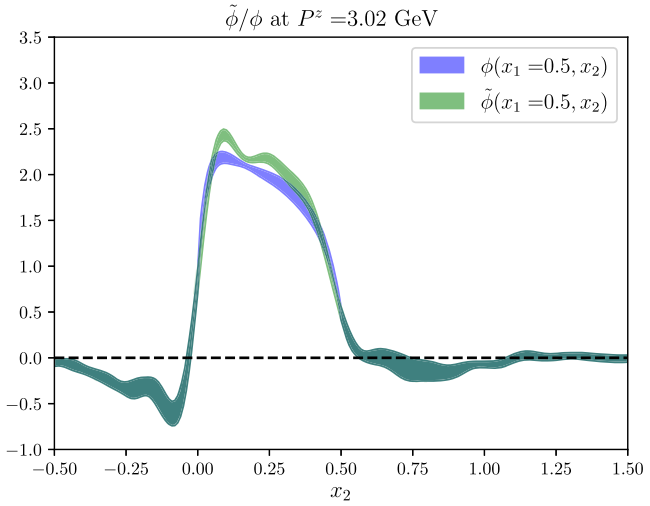

FIG. 12. Comparison of the Λ LCDA $\phi(x_1, x_2, \mu, P^z)$ and the quasi-DA $\tilde{\phi}(x_1, x_2, \mu, P^z)$ at hadron momentum $P^z = 3.02$ GeV as a function of x_2 at $x_1 = 0.5$.

attributed to the SU(3) difference between the u/d and s quarks. Additionally, a small but nonvanishing tail of $\tilde{\phi}(x_1, x_2, \mu, P^z)$ appears in the unphysical region, defined as $\{(x_1, x_2)|x_1, x_2 < 0, \text{ or } x_1, x_2 > 1, \text{ or } x_1 + x_2 > 1\}$. Such behaviors might be caused by higher-twist contributions or other systematic uncertainties.

F. Results for baryon LCDAs and phenomenological impact

Direct implementation of the matching procedure for the two-dimensional baryon DA encounters great challenges. Specifically, one must address the double-plus functions as defined in Eq. (23), which are likely to have divergences at several end points. Fortunately, by applying the properties of plus functions, one can simplify the matching formula in Eq. (24). The formulation of the function $[f(x_1, x_2, y_1, y_2)]_{\oplus}$ in Eq. (23) incorporates three Dirac δ functions per term, thereby necessitating only a single integration for each term to determine $\phi(x_1, x_2)$ from $\tilde{\phi}(x_1, x_2)$. This streamlined approach is pursued in the subsequent analysis. More details are collected in Appendix A.

Moreover, to retain the information of quasi-DA in the unphysical region, it is useful to apply the δ function in this region, together with one-loop corrections for the matching kernel in the physical region $\Lambda: \{(x_1, x_2)|0 < x_1 < 1, 0 < x_2 < 1 - x_1\}$. Then the one-loop corrections become

$$\tilde{c}^{(1)}(x_1, x_2, y_1, y_2) = \begin{cases} c^{(1)}(x_1, x_2, y_1, y_2), & x_1, x_2 \in \Lambda, \\ \delta(x_1 - y_1)\delta(x_1 - y_2), & x_1, x_2 \notin \Lambda. \end{cases} \tag{27}$$

We then compare the quasi- and light cone DAs to investigate the impact of one-loop corrections on the matching coefficient, as depicted in Fig. 12. The shown example has $x_1 = 0.5$ and $P^z = 3.02$ GeV, which corresponds to the orange band in Fig. 11. At leading order, the matching coefficient simplifies to a Dirac δ function, suggesting that the discrepancies observed between the quasi-DA and the light cone DA are primarily attributable to one-loop corrections. Consequently, this analysis underscores that the one-loop corrections to the matching coefficient are not significant, but instrumental in attenuating the oscillations observed.

Next, we investigate the large-momentum limit of our findings by analyzing the LCDA $\Phi(x_1, x_2, P^z)$ obtained at three distinct momenta. These values stem from the quasi-DA $\tilde{\Phi}(x_1, x_2, P^z)$ through the matching process outlined previously. To address the power corrections proportional to $1/(P^z)^2$, we perform an extrapolation as P^z approaches infinity for $\phi(x_1, x_2, P^z)$ at three specific hadron momenta: $P^z = \{2.58, 3.02, 3.58\}$ GeV, as depicted by the equation

$$\phi(x, P_z) = \phi(x, P_z \to \infty) + \frac{c_2(x)}{(P_z)^2} + \frac{c_4(x)}{(P_z)^4}. \tag{28}$$

In this procedure we have quantified the systematic uncertainty as the variance between the LCDA at the highest momentum, $P^z = 3.58$ GeV, and the limit as P_z tends to infinity,

$$\sigma_{\text{sys}} = |\phi(x, P^z \to \infty) - \phi(x, P^z = 3.58 \text{ GeV})|. \tag{29}$$

The LCDA $\phi(x_1, x_2, P^z)$ outcomes at three hadron momenta, along with the extrapolated results, are depicted in Fig. 13. Notably, $\phi(x_1, x_2, P^z)$ at $P^z = 3.52$ GeV demonstrates a deviation from the results at lower momenta, $P^z = \{2.58, 3.02\}$ GeV.

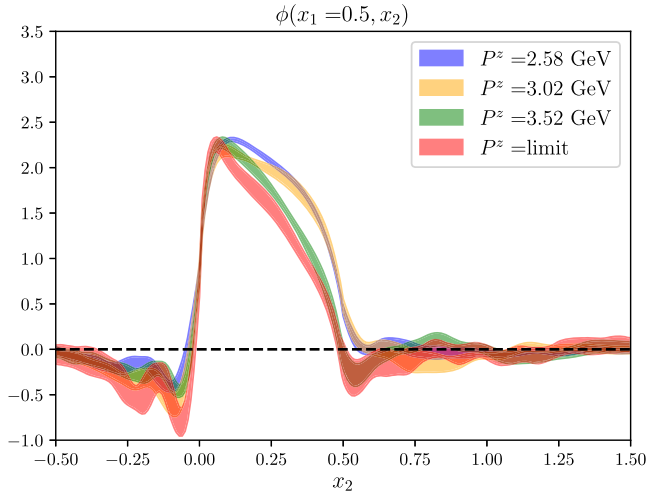

FIG. 13. Large-momentum limit for the Λ LCDA, including results at $P^z = \{2.58, 3.02, 3.58\}$ GeV and the extrapolated one.

The final results for the Λ LCDA, $\phi(x_1, x_2)$ in the infinite momentum limit are showcased in Fig. 14. The upper panel of this figure displays $\phi(x_1, x_2)$ as a function of x_2 at fixed $x_1 = 0.25$, 0.5, and 0.75. The lower panel is a heat map to visually depict the distribution of LCDA across the x_1-x_2 plane. Statistical uncertainties are calculated from bootstrap samples of all measurements. Systematic uncertainties are attributed to various factors including the choice of fitting range for extrapolation, the selection of regions for utilizing extrapolated data, and the adoption of the infinite momentum limit.

The result of LCDA $\phi(x_1, x_2)$ refers to the leading-twist LCDA A for the Λ baryon, which is illustrated in Fig. 14. Considering Eq. (20), owing to power corrections represented as $\Lambda^2_{\rm QCD}/(x_{1,2}P^z)^2$ and $\Lambda^2_{\rm QCD}/[(1-x_1-x_2)P^z]^2$, a region of unreliability emerges. This region is estimated to be $\{0 < x_{1,2} < 0.1, 0.9 < x_1 < 1, 0.9 - x_1 < x_2 < 1 - x_1\}$. According to Fig. 14, it exhibits two principal characteristics:

(i) In the unphysical region, $\{x_2 < 0$ or $x_2 > 1 - x_1\}$, the LCDA $\phi(x_1, x_2)$ tends toward zero, likely influenced by the employment of large hadron momenta, the infinite momentum limit, and extensive λ extrapolation.

(ii) The LCDA $\phi(x_1, x_2)$ shows a dominant distribution in the regions where $x_1, x_2 \to 0$, aligning with observations in the quasi-DA. This might indicate a substantial contribution from the strange (s) quark to the momentum fraction in the Λ baryon or require a more systematic treatment of power corrections at long distances, meriting further investigation.

As a phenomenological application, we apply our preliminary result to calculate the $\Lambda_b \to \Lambda$ form factors. We adopt the results using light cone sum rules [24] and calculate the form factor g_2. To assist this calculation, a parametrization of the Λ LCDA is used by

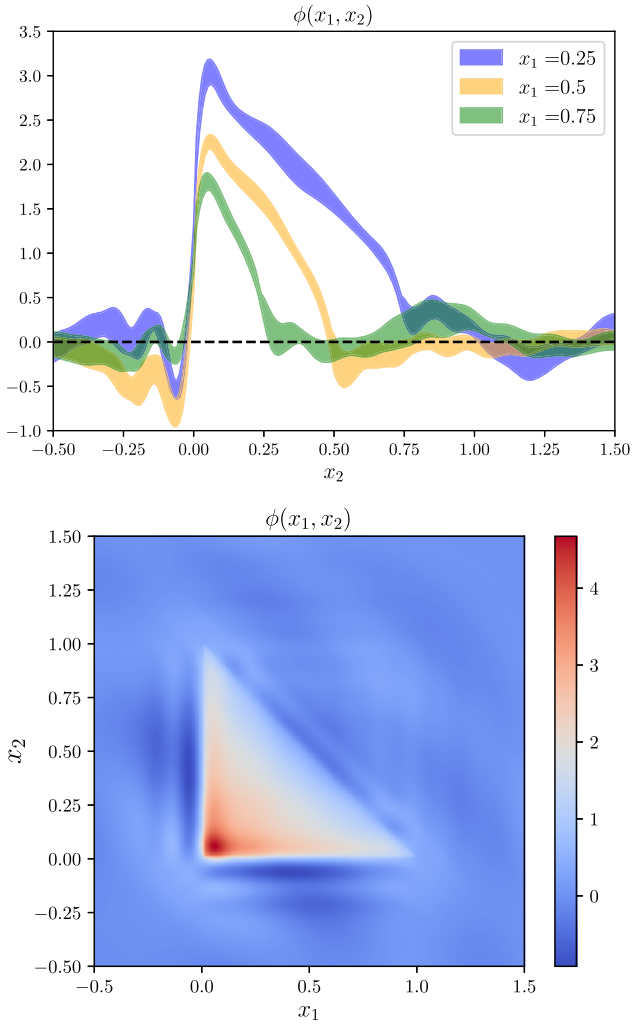

FIG. 14. Upper: the Λ LCDA at $x_1 = 0.25, 0.5, 0.75$ as a function of x_2 in the infinite momentum limit. Lower: the two-dimensional distributions of x_1 and x_2 but only central value of Λ LCDA in infinite momentum limit. The unreliable region is estimated as $\{0 < x_{1,2} < 0.1, 0.9 < x_1 < 1, 0.9 - x_1 < x_2 < 1 - x_1\}$.

$$\phi(x_1, x_2) = C x_1^{d_1} x_2^{d_1} (1 - x_1 - x_2)^{d_2}, \tag{30}$$

where d_1, d_2, and C are parameters to be fitted. To optimize the results, we fit $\phi(x_1, x_2)$ within the medium region to avoid higher power corrections, yielding $d_1 = 0.90(36)$ and $d_2 = 1.59(40)$. It should be noted that this result obtained by fitting in the intermediate region of LCDA in momentum space differs significantly from the results in Table II which were obtained by fitting coordinate space quasi-DA at large z. This also implies that the parametrization model is not entirely reasonable. For the LCDA results obtained from LaMET, it is preferable to directly substitute the numerical results. Implementing these values in the calculation of the form factor, we obtain $g_2 = -0.0169(31)$ at Borel mass $M_B^2 = 3$ GeV^2. Compared to the result in Ref. [24] $g_2 = -0.02364$ where an asymptotic

form is used for the LCDA $\phi(x_1,x_2)=120x_1x_2(1-x_1-x_2)$, our findings on the leading-twist LCDAs ϕ_A can make an reduction of the form factor by approximately 20%. This might have an impact on weak decays like $\Lambda_b \to \Lambda\ell^+\ell^-$, where previous theoretical predictions overshoot the experimental data on $\Lambda_b \to \Lambda\mu^+\mu^-$ [141]. These changes from the baryon LCDA might help resolve the tensions between experimental measurements and theoretical prediction, though this is very preliminary. Moreover, once the form factors at large recoil and low q^2 are precisely predicted, a combined analysis with the lattice QCD results for the form factors at low recoil [27,28] allows one to access the form factors in the whole kinematic region.

IV. CONCLUSION AND PROSPECTS

We have presented the first attempt to calculate the baryon light cone distribution amplitude using LaMET on the lattice, taking the structure of a major contribution in the leading twist of Λ baryon as an example. We discuss the challenges faced by the hybrid scheme in baryon distribution amplitudes and employed a simplified ratio as a preliminary attempt. Additionally, we simplify the parametrization used for the large λ extrapolation. For the lattice numerical simulations, we utilize one configuration with lattice spacing of 0.077 fm and pion mass of 303 MeV, performing calculations at three different momentum values for large-momentum extrapolation.

From our numerical results, we observe that the quasi-DA in coordinate space aligns with our expectations regarding its analytic properties. The final distribution of the LCDA also reflects the fundamental characteristics of baryons. However, there are some issues in the numerical results to be improved in the future, such as the renormalization scheme. Furthermore, our results represent only a nonphysical pion mass with only one lattice spacing calculation, lacking comprehensive estimates of discretization errors and other systematic uncertainties.

Therefore, to achieve accurate and precise calculations of the baryon LCDA in future studies, we need to employ more configurations with smaller lattice spacings and higher statistics, while also adopting a more robust renormalization scheme and numerical analysis processes. A reliable computation of the baryon LCDA will significantly enhance phenomenological studies.

ACKNOWLEDGMENTS

We thank Yu Jia, Yu-Ming Wang, and Fu-Sheng Yu for useful discussions. We thank the CLQCD collaborations for providing us the gauge configurations with dynamical fermions [128], which are generated on the HPC Cluster of ITP-CAS, the Southern Nuclear Science Computing Center (SNSC), the Siyuan-1 cluster supported by the Center for High Performance Computing at Shanghai Jiao Tong University, and the Dongjiang Yuan Intelligent Computing Center. This work is supported in part by Guangdong Major Project of Basic and Applied Basic Research No. 2020B0301030008, Natural Science Foundation of China under Grants No. 12125503, No. 12335003, No. 12375069, No. 12105247, No. 12275277, No. 12205106, No. 12175073, No. 12222503, No. 12147140, No. 12205180, No. 12375080, No. 11975051, No. 12293060, No. 12293062, No. 12047503, and No. 12275364. J. H. Z is also supported by CUHK-Shenzhen under Grant No. UDF01002851. A. S., W. W., Y. Y., and J. H. Z. were also partially supported by a NSFC-DFG joint grant under Grant No. 12061131006 and SCHA 458/22. J. Z. is also partially supported by the Project funded by China Postdoctoral Science Foundation under Grant No. 2022M712088. The computations in this paper were run on the Siyuan-1 cluster supported by the Center for High Performance Computing at Shanghai Jiao Tong University and Advanced Computing East China Sub-center. This work was partially supported by SJTU Kunpeng and Ascend Center of Excellence. The LQCD simulations were performed using the Chroma software suite [142] and QUDA [143–145] through the HIP programming model [146].

DATA AVAILABILITY

The data that support the findings of this article are not publicly available upon publication because it is not technically feasible and/or the cost of preparing, depositing, and hosting the data would be prohibitive within the terms of this research project. The data are available from the authors upon reasonable request.

APPENDIX A: DETAILED EXPRESSIONS FOR MATCHING KERNEL

The next-to-leading order of ratio scheme matching kernel $c^{(1)}(x_1,x_2,y_1,y_2)$ is given by the double-plus function $f_\oplus$,

$$c^{(1)}(x_1,x_2,y_1,y_2) = [f(x_1,x_2,y_1,y_2)]_\oplus = f(x_1,x_2,y_1,y_2) - \delta(x_1-y_1)\delta(x_2-y_2)\int_{-\infty}^{\infty} dt_1 \int_{-\infty}^{\infty} dt_2 f(t_1,t_2,y_1,y_2), \tag{A1}$$

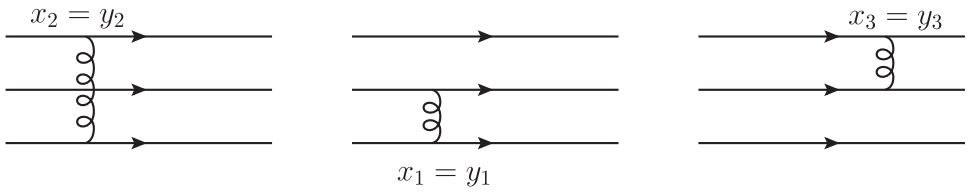

FIG. 15. The Feynman diagram corresponds to three terms in one-loop matching coefficient.

with

$$f(x_1,x_2,y_1,y_2) = \delta(x_2-y_2)\left[\frac{1}{4}Q_2(x_1,x_2,y_1,y_2)+\frac{7}{8}\frac{1}{|x_1-y_1|}\right]+\delta(x_1-y_1)\left[\frac{1}{4}Q_2(x_2,x_1,y_2,y_1)+\frac{7}{8}\frac{1}{|x_2-y_2|}\right]$$
$$+\delta(x_1+x_2-y_1-y_2)\left[\frac{1}{4}Q_3(x_1,x_2,y_1,y_2)+\frac{1}{4}Q_3(x_2,x_1,y_2,y_1)+\frac{3}{2}\frac{1}{|x_1-x_2-y_1+y_2|}\right], \tag{A2}$$

where $f(x_1,x_2,y_1,y_2)$ is divided into three terms, each of which includes a Dirac δ function. As displayed in Fig. 15, these three terms correspond to the one-loop contributions of two pairs of quarks exchanging gluons, where the spectator quark is represented by the Dirac δ function.

The functions Q_2 and Q_3 are

$$Q_2(x_1,x_2,y_1,y_2) = \begin{cases} \frac{(x_1+y_1)(x_3+y_3)\ln\frac{y_1-x_1}{-x_1}}{y_1y_3(y_1-x_1)} - \frac{x_3(x_1+y_1+2y_3)\ln\frac{x_3}{-x_1}}{y_3(y_1-x_1)(y_1+y_3)}, & x_1<0 \\ \frac{(x_1-3y_1-2y_3)x_1}{y_1(x_3-y_3)(y_1+y_3)} - \frac{[(x_3-y_3)^2-2x_3y_1]\ln\frac{x_3-y_3}{x_3}}{(x_3-y_3)y_1y_3} + \frac{2x_1\ln\frac{4x_1(x_3-y_3)p_z^2}{\mu^2}}{y_1(x_3-y_3)} + \frac{x_1\ln\frac{4x_1x_3p_z^2}{\mu^2}}{y_1(y_1+y_3)}, & 0<x_1<y_1 \\ \frac{(x_3-2y_1-3y_3)x_3}{y_3(x_1-y_1)(y_1+y_3)} - \frac{[(x_1-y_1)^2-2x_1y_3]\ln\frac{x_1-y_1}{x_1}}{(x_1-y_1)y_1y_3} + \frac{2x_3\ln\frac{4x_3(x_1-y_1)p_z^2}{\mu^2}}{y_3(x_1-y_1)} + \frac{x_3\ln\frac{4x_1x_3p_z^2}{\mu^2}}{y_3(y_1+y_3)}, & y_1<x_1<y_1+y_3 \\ \frac{(x_1+y_1)(x_3+y_3)\ln\frac{y_3-x_3}{-x_3}}{y_1y_3(y_3-x_3)} - \frac{x_1(x_3+2y_1+y_3)\ln\frac{x_1}{-x_3}}{y_1(y_3-x_3)(y_1+y_3)}, & x_1>y_1+y_3, \end{cases} \tag{A3}$$

$$Q_3(x_1,x_2,y_1,y_2) = \begin{cases} \frac{(x_1x_2+y_1y_2)\ln\frac{x_2-y_2}{x_2}}{y_1y_2(x_2-y_2)} - \frac{x_1(x_2+y_1)\ln\frac{-x_1}{x_2}}{y_1(x_2-y_2)(y_1+y_2)}, & x_1<0 \\ \frac{1}{x_1-y_1} + \frac{2x_1+x_2}{y_1(y_1+y_2)} + \frac{[(x_1+y_2)y_1-x_1^2]\ln\frac{x_2-y_2}{x_2}}{y_1y_2(x_2-y_2)} + \frac{x_1\ln\frac{4x_1(x_2-y_2)p_z^2}{\mu^2}}{y_1(x_2-y_2)} + \frac{x_1\ln\frac{4x_1x_2p_z^2}{\mu^2}}{y_1(y_1+y_2)}, & 0<x_1<y_1 \\ \frac{1}{x_2-y_2} + \frac{x_1+2x_2}{y_2(y_1+y_2)} + \frac{[(x_2+y_1)y_2-x_2^2]\ln\frac{x_1-y_1}{x_1}}{y_1y_2(x_1-y_1)} + \frac{x_2\ln\frac{4x_2(x_1-y_1)p_z^2}{\mu^2}}{y_2(x_1-y_1)} + \frac{x_2\ln\frac{4x_1x_2p_z^2}{\mu^2}}{y_2(y_1+y_2)}, & y_1<x_1<y_1+y_2 \\ \frac{(x_1x_2+y_1y_2)\ln\frac{x_1-y_1}{x_1}}{y_1y_2(x_1-y_1)} - \frac{x_2(x_1+y_2)\ln\frac{-x_2}{x_1}}{y_2(x_1-y_1)(y_1+y_2)}, & x_1>y_1+y_2. \end{cases} \tag{A4}$$

APPENDIX B: QUASI-DA IN COORDINATE SPACE

In Sec. III C, the behavior of the quasi-DA in coordinate space, $\tilde{\Phi}(z_1,z_2)$ is discussed. However, this discussion encompasses only a subset of all examples. As a supplement, we present the remaining cases here, including $P^z = \{2.58, 3.02, 3.52\}$ GeV for all z_1, illustrated in Figs. 16–18. Because of significant uncertainties for $z_1 \geq 8a$, this region does not yield relevant information. Therefore, only $z_1 \leq 8a$ is displayed.

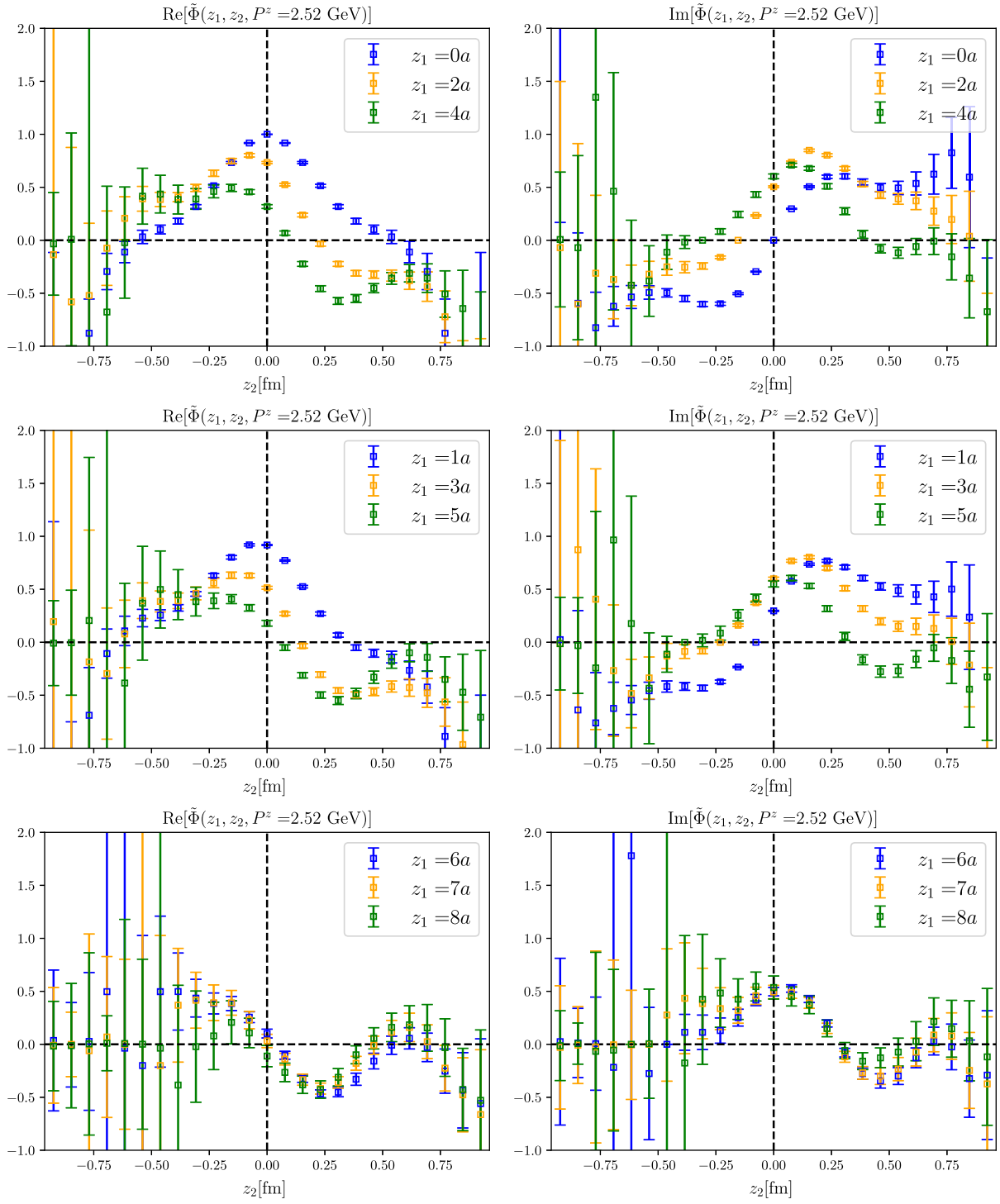

FIG. 16. The figures show the behavior of $\tilde{\Phi}(z_1, z_2)$ at all fixed $z_1 \leq 8a$ as a function of z_2. These are cases at $P^z = 2.58$ GeV.

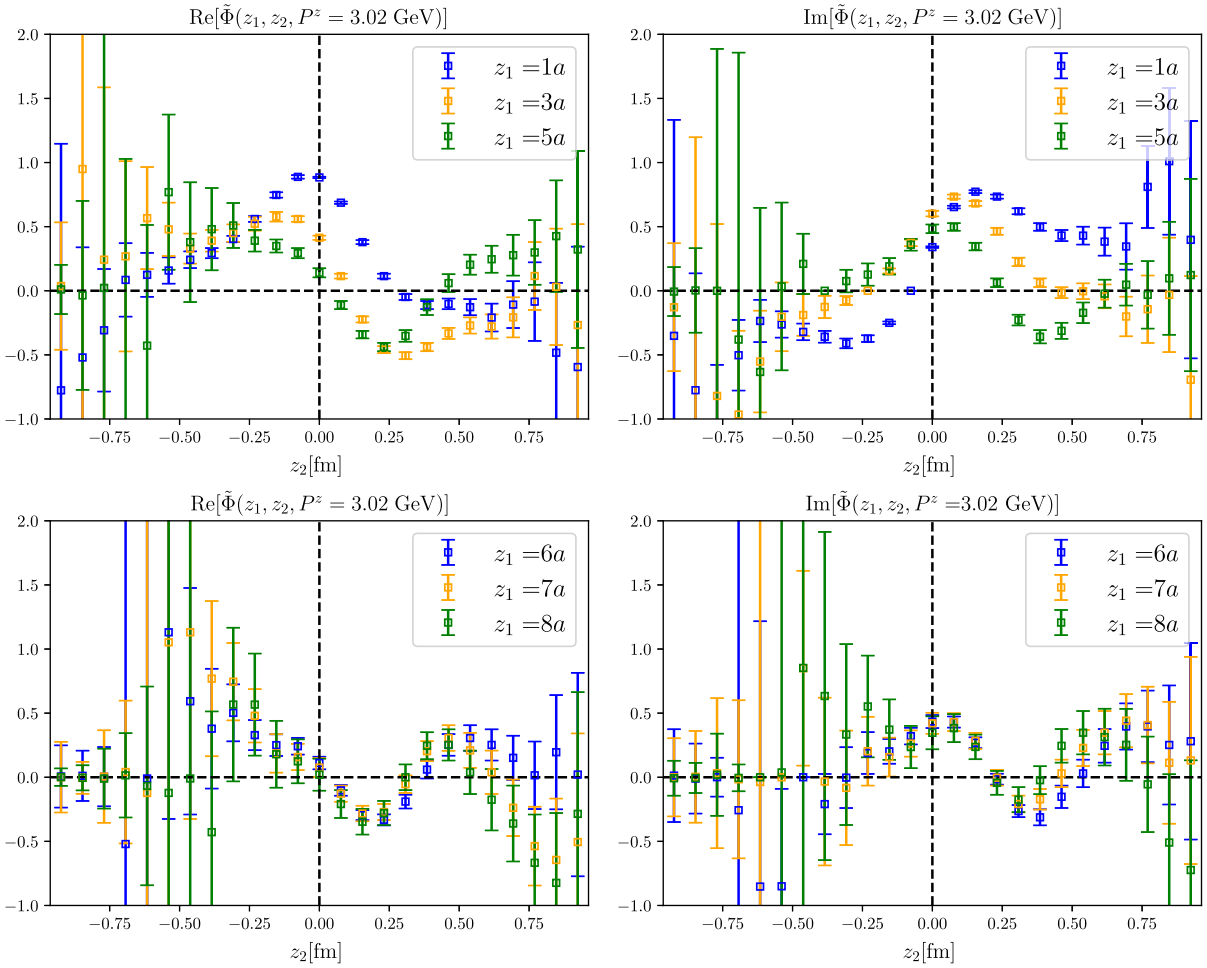

FIG. 17. The figures show the behavior of $\tilde{\Phi}(z_1, z_2)$ at all fixed $z_1 \leq 8a$ as a function of z_2. These are supplement cases to Fig. 7 in the main text at $P^z = 3.02$ GeV.

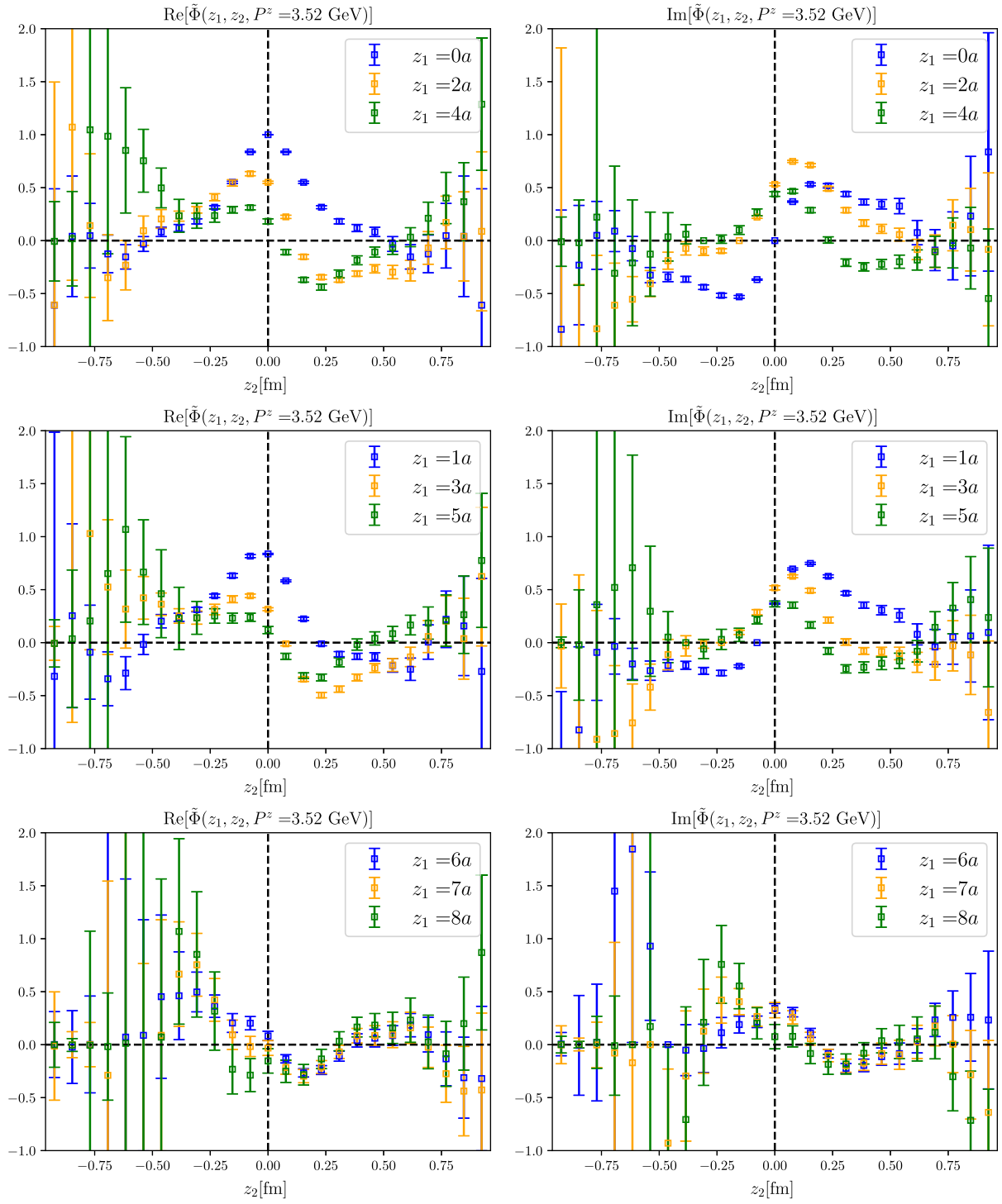

FIG. 18. The figures show the behavior of $\tilde{\Phi}(z_1, z_2)$ at all fixed $z_1 \leq 8a$ as a function of z_2. These are cases at $P^z = 3.53$ GeV.

[1] G. P. Lepage and S. J. Brodsky, Phys. Rev. D **22**, 2157 (1980).
[2] V. L. Chernyak and A. R. Zhitnitsky, Phys. Rep. **112**, 173 (1984).
[3] J. J. Han, Y. Li, H. n. Li, Y. L. Shen, Z. J. Xiao, and F. S. Yu, Eur. Phys. J. C **82**, 686 (2022).
[4] Y. M. Wang and Y. L. Shen, J. High Energy Phys. 02 (2016) 179.
[5] R. Aaij *et al.* (LHCb Collaboration), Nat. Phys. **13**, 391 (2017).
[6] R. Aaij *et al.* (LHCb Collaboration), arXiv:2411.15441.
[7] G. S. Bali, V.M. Braun, M. Göckeler, M. Gruber, F. Hutzler, P. Korcyl, B. Lang, and A. Schäfer (RQCD Collaboration), Phys. Lett. B **774**, 91 (2017).
[8] G. S. Bali, V. M. Braun, S. Bürger, M. Göckeler, M. Gruber, F. Hutzler, P. Korcyl, A. Schäfer, A. Sternbeck, and P. Wein (RQCD Collaboration), J. High Energy Phys. 08 (2019) 065.
[9] J. H. Zhang, J. W. Chen, X. Ji, L. Jin, and H. W. Lin, Phys. Rev. D **95**, 094514 (2017).
[10] J. H. Zhang *et al.* (LP3 Collaboration), Nucl. Phys. **B939**, 429 (2019).
[11] R. Zhang, C. Honkala, H. W. Lin, and J. W. Chen, Phys. Rev. D **102**, 094519 (2020).
[12] X. Gao, A. D. Hanlon, N. Karthik, S. Mukherjee, P. Petreczky, P. Scior, S. Syritsyn, and Y. Zhao, Phys. Rev. D **106**, 074505 (2022).
[13] J. Holligan, X. Ji, H. W. Lin, Y. Su, and R. Zhang, Nucl. Phys. **B993**, 116282 (2023).
[14] J. Hua, M.-H. Chu, P. Sun, W. Wang, J. Xu, Y.-B. Yang, J.-H. Zhang, and Q.-A. Zhang (Lattice Parton Collaboration), Phys. Rev. Lett. **127**, 062002 (2021).
[15] J. Hua *et al.* (Lattice Parton Collaboration), Phys. Rev. Lett. **129**, 132001 (2022).
[16] E. Baker, D. Bollweg, P. Boyle, I. Cloët, X. Gao, S. Mukherjee, P. Petreczky, R. Zhang, and Y. Zhao, J. High Energy Phys. 07 (2024) 211.
[17] I. Cloet, X. Gao, S. Mukherjee, S. Syritsyn, N. Karthik, P. Petreczky, R. Zhang, and Y. Zhao, Phys. Rev. D **110**, 114502 (2024).
[18] V. L. Chernyak, A. A. Ogloblin, and I. R. Zhitnitsky, Yad. Fiz. **48**, 1410 (1988).
[19] A. V. Radyushkin, Nucl. Phys. **A532**, 141 (1991).
[20] J. Bolz and P. Kroll, Z. Phys. A **356**, 327 (1996).
[21] V. M. Braun, A. Lenz, N. Mahnke, and E. Stein, Phys. Rev. D **65**, 074011 (2002).
[22] I. V. Anikin, V. M. Braun, and N. Offen, Phys. Rev. D **88**, 114021 (2013).
[23] G. Bell, T. Feldmann, Y. M. Wang, and M. W. Y. Yip, J. High Energy Phys. 11 (**2013**) 191.
[24] Y. m. Wang, Y. Li, and C. D. Lu, Eur. Phys. J. C **59**, 861 (2009).
[25] Z. Rui, C. Q. Zhang, J. M. Li, and M. K. Jia, Phys. Rev. D **106**, 053005 (2022).
[26] W. Wang, Phys. Lett. B **708**, 119 (2012).
[27] W. Detmold, C. J. D. Lin, S. Meinel, and M. Wingate, Proc. Sci. LATTICE2012 (**2012**) 123 [arXiv:1211.5127].
[28] W. Detmold, C. J. D. Lin, S. Meinel, and M. Wingate, Phys. Rev. D **87**, 074502 (2013).
[29] G. S. Bali, V. M. Braun, M. Göckeler, M. Gruber, F. Hutzler, A. Schäfer, R. W. Schiel, J. Simeth, W. Söldner, A. Sternbeck *et al.*, J. High Energy Phys. 02 (2016) 070.
[30] G. S. Bali *et al.* (RQCD Collaboration), Eur. Phys. J. A **55**, 116 (2019).
[31] W. Chen, F. Feng, and Y. Jia, arXiv:2406.19994.
[32] Y. K. Huang, B. X. Shi, Y. M. Wang, and X. C. Zhao, arXiv:2407.18724.
[33] X. Ji, Phys. Rev. Lett. **110** (2013), 262002.
[34] X. Ji, Sci. China Phys. Mech. Astron. **57**, 1407 (2014).
[35] X. Ji, Y. S. Liu, Y. Liu, J. H. Zhang, and Y. Zhao, Rev. Mod. Phys. **93**, 035005 (2021).
[36] X. Xiong, X. Ji, J. H. Zhang, and Y. Zhao, Phys. Rev. D **90**, 014051 (2014).
[37] H. W. Lin, J. W. Chen, S. D. Cohen, and X. Ji, Phys. Rev. D **91**, 054510 (2015).
[38] C. Alexandrou, K. Cichy, V. Drach, E. Garcia-Ramos, K. Hadjiyiannakou, K. Jansen, F. Steffens, and C. Wiese, Phys. Rev. D **92**, 014502 (2015).
[39] J. W. Chen, S. D. Cohen, X. Ji, H. W. Lin, and J. H. Zhang, Nucl. Phys. **B911**, 246 (2016).
[40] C. Alexandrou, K. Cichy, M. Constantinou, K. Hadjiyiannakou, K. Jansen, F. Steffens, and C. Wiese, Phys. Rev. D **96**, 014513 (2017).
[41] C. Alexandrou, K. Cichy, M. Constantinou, K. Jansen, A. Scapellato, and F. Steffens, Phys. Rev. Lett. **121**, 112001 (2018).
[42] J. W. Chen, L. Jin, H. W. Lin, Y. S. Liu, Y. B. Yang, J. H. Zhang, and Y. Zhao, arXiv:1803.04393.
[43] H. W. Lin, J. W. Chen, X. Ji, L. Jin, R. Li, Y. S. Liu, Y. B. Yang, J. H. Zhang, and Y. Zhao, Phys. Rev. Lett. **121**, 242003 (2018).
[44] Y. S. Liu *et al.* (Lattice Parton Collaboration), Phys. Rev. D **101**, 034020 (2020).
[45] C. Alexandrou, K. Cichy, M. Constantinou, K. Jansen, A. Scapellato, and F. Steffens, Phys. Rev. D **98**, 091503 (2018).
[46] Y. S. Liu, J. W. Chen, L. Jin, R. Li, H. W. Lin, Y. B. Yang, J. H. Zhang, and Y. Zhao, arXiv:1810.05043.
[47] J. H. Zhang, J. W. Chen, L. Jin, H. W. Lin, A. Schäfer, and Y. Zhao, Phys. Rev. D **100**, 034505 (2019).
[48] T. Izubuchi, X. Ji, L. Jin, I. W. Stewart, and Y. Zhao, Phys. Rev. D **98**, 056004 (2018).
[49] T. Izubuchi, L. Jin, C. Kallidonis, N. Karthik, S. Mukherjee, P. Petreczky, C. Shugert, and S. Syritsyn, Phys. Rev. D **100**, 034516 (2019).
[50] C. Shugert, X. Gao, T. Izubichi, L. Jin, C. Kallidonis, N. Karthik, S. Mukherjee, P. Petreczky, S. Syritsyn, and Y. Zhao, arXiv:2001.11650.
[51] Y. Chai, Y. Li, S. Xia, C. Alexandrou, K. Cichy, M. Constantinou, X. Feng, K. Hadjiyiannakou, K. Jansen, G. Koutsou*et al.*, Phys. Rev. D **102**, 014508 (2020).
[52] H. W. Lin, J. W. Chen, Z. Fan, J. H. Zhang, and R. Zhang, Phys. Rev. D **103**, 014516 (2021).
[53] Z. Fan, X. Gao, R. Li, H. W. Lin, N. Karthik, S. Mukherjee, P. Petreczky, S. Syritsyn, Y. B. Yang, and R. Zhang, Phys. Rev. D **102**, 074504 (2020).
[54] X. Gao, K. Lee, S. Mukherjee, C. Shugert, and Y. Zhao, Phys. Rev. D **103**, 094504 (2021).
[55] X. Gao, A. D. Hanlon, S. Mukherjee, P. Petreczky, P. Scior, S. Syritsyn, and Y. Zhao, Phys. Rev. Lett. **128**, 142003 (2022).

[56] X. Gao, A. D. Hanlon, N. Karthik, S. Mukherjee, P. Petreczky, P. Scior, S. Shi, S. Syritsyn, Y. Zhao, and K. Zhou, Phys. Rev. D **106**, 114510 (2022).
[57] Y. Su, J. Holligan, X. Ji, F. Yao, J. H. Zhang, and R. Zhang, Nucl. Phys. **B991**, 116201 (2023).
[58] F. Yao *et al.* (Lattice Parton Collaboration), Phys. Rev. Lett. **131**, 261901 (2023).
[59] X. Gao, A. D. Hanlon, J. Holligan, N. Karthik, S. Mukherjee, P. Petreczky, S. Syritsyn, and Y. Zhao, Phys. Rev. D **107**, 074509 (2023).
[60] C. Y. Chou and J. W. Chen, Phys. Rev. D **106**, 014507 (2022).
[61] X. Gao, W. Y. Liu, and Y. Zhao, Phys. Rev. D **109**, 094506 (2024).
[62] X. Gao, A. D. Hanlon, S. Mukherjee, P. Petreczky, Q. Shi, S. Syritsyn, and Y. Zhao, Phys. Rev. D **109**, 054506 (2024).
[63] C. Chen, L. Liu, P. Sun, Y. B. Yang, Y. Geng, F. Yao, J. H. Zhang, and K. Zhang, arXiv:2408.12819.
[64] J. Holligan and H. W. Lin, J. Phys. G **51**, 065101 (2024).
[65] J. Holligan and H. W. Lin, Phys. Lett. B **854**, 138731 (2024).
[66] W. Wang, S. Zhao, and R. Zhu, Eur. Phys. J. C **78**, 147 (2018).
[67] W. Wang and S. Zhao, J. High Energy Phys. 05 (2018) 142.
[68] Z. Y. Fan, Y. B. Yang, A. Anthony, H. W. Lin, and K. F. Liu, Phys. Rev. Lett. **121**, 242001 (2018).
[69] W. Wang, J. H. Zhang, S. Zhao, and R. Zhu, Phys. Rev. D **100**, 074509 (2019).
[70] W. Good, K. Hasan, and H. W. Lin, arXiv:2409.02750.
[71] J. W. Chen, H. W. Lin, and J. H. Zhang, Nucl. Phys. **B952**, 114940 (2020).
[72] C. Alexandrou, K. Cichy, M. Constantinou, K. Hadjiyiannakou, K. Jansen, A. Scapellato, and F. Steffens, Proc. Sci. LATTICE2019 (**2019**) 036 [arXiv:1910.13229].
[73] H. W. Lin, Phys. Rev. Lett. **127**, 182001 (2021).
[74] C. Alexandrou, K. Cichy, M. Constantinou, K. Hadjiyiannakou, K. Jansen, A. Scapellato, and F. Steffens, Phys. Rev. Lett. **125**, 262001 (2020).
[75] H. W. Lin, Phys. Lett. B **824**, 136821 (2022).
[76] A. Scapellato, C. Alexandrou, K. Cichy, M. Constantinou, K. Hadjiyiannakou, K. Jansen, and F. Steffens, Rev. Mex. Fis. Suppl. **3**, 0308104 (2022).
[77] S. Bhattacharya, K. Cichy, M. Constantinou, J. Dodson, X. Gao, A. Metz, S. Mukherjee, A. Scapellato, F. Steffens, and Y. Zhao, Phys. Rev. D **106**, 114512 (2022).
[78] S. Bhattacharya, K. Cichy, M. Constantinou, J. Dodson, A. Metz, A. Scapellato, and F. Steffens, Phys. Rev. D **108**, 054501 (2023).
[79] S. Bhattacharya, K. Cichy, M. Constantinou, J. Dodson, X. Gao, A. Metz, J. Miller, S. Mukherjee, P. Petreczky, F. Steffens *et al.*, Phys. Rev. D **109**, 034508 (2024).
[80] H. W. Lin, Phys. Lett. B **846**, 138181 (2023).
[81] J. Holligan and H. W. Lin, Phys. Rev. D **110**, 034503 (2024).
[82] H. T. Ding, X. Gao, S. Mukherjee, P. Petreczky, Q. Shi, S. Syritsyn, and Y. Zhao, arXiv:2407.03516.
[83] Y. S. Liu, W. Wang, J. Xu, Q. A. Zhang, S. Zhao, and Y. Zhao, Phys. Rev. D **99**, 094036 (2019).
[84] Z. F. Deng, C. Han, W. Wang, J. Zeng, and J. L. Zhang, J. High Energy Phys. 07 (**2023**) 191.
[85] C. Han, Y. Su, W. Wang, and J. L. Zhang, J. High Energy Phys. 12 (2023) 044.
[86] C. Han and J. Zhang, Phys. Rev. D **109**, 014034 (2024).
[87] C. Han, W. Wang, J. Zeng, and J. L. Zhang, J. High Energy Phys. 07 (2024) 019.
[88] W. Wang, Y. M. Wang, J. Xu, and S. Zhao, Phys. Rev. D **102**, 011502 (2020).
[89] S. Zhao and A. V. Radyushkin, Phys. Rev. D **103**, 054022 (2021).
[90] J. Xu, X. R. Zhang, and S. Zhao, Phys. Rev. D **106**, L011503 (2022).
[91] J. Xu and X. R. Zhang, Phys. Rev. D **106**, 114019 (2022).
[92] S. M. Hu, W. Wang, J. Xu, and S. Zhao, Phys. Rev. D **109**, 034001 (2024).
[93] S. M. Hu, J. Xu, and S. Zhao, Eur. Phys. J. C **84**, 502 (2024).
[94] X. Y. Han, J. Hua, X. Ji, C. D. Lü, W. Wang, J. Xu, Q. A. Zhang, and S. Zhao, arXiv:2403.17492.
[95] C. Han, W. Wang, J. L. Zhang, and J. H. Zhang, Phys. Rev. D **110**, 094038 (2024).
[96] Z. F. Deng, W. Wang, Y. B. Wei, and J. Zeng, Phys. Rev. D **110**, 114006 (2024).
[97] X. Y. Han, J. Hua, X. Ji, C. D. Lü, A. Schäfer, Y. Su, W. Wang, J. Xu, Y. Yang, J. H. Zhang *et al.*, arXiv:2410.18654.
[98] X. Ji, P. Sun, X. Xiong, and F. Yuan, Phys. Rev. D **91**, 074009 (2015).
[99] P. Shanahan, M. L. Wagman, and Y. Zhao, Phys. Rev. D **101**, 074505 (2020).
[100] P. Shanahan, M. Wagman, and Y. Zhao, Phys. Rev. D **102**, 014511 (2020).
[101] Q. A. Zhang *et al.* (Lattice Parton Collaboration), Phys. Rev. Lett. **125**, 192001 (2020).
[102] X. Ji and Y. Liu, Phys. Rev. D **105**, 076014 (2022).
[103] M. H. Chu *et al.* (Lattice Parton Collaboration (LPC)), Phys. Rev. D **106**, 034509 (2022).
[104] Y. Liu, Acta Phys. Pol. B **53**, 4 (2022).
[105] K. Zhang, X. Ji, Y.-B. Yang, F. Yao, and J.-H. Zhang (Lattice Parton Collaboration (LPC)), Phys. Rev. Lett. **129**, 082002 (2022).
[106] Z. F. Deng, W. Wang, and J. Zeng, J. High Energy Phys. 09 (2022) 046.
[107] R. Zhu, Y. Ji, J. H. Zhang, and S. Zhao, J. High Energy Phys. 02 (2023) 114.
[108] J. C. He, M.-H. Chu, J. Hua, X. Ji, A. Schäfer, Y. Su, W. Wang, Y.-B. Yang, J.-H. Zhang, and Q.-A. Zhang (Lattice Parton Collaboration (LPC)), Phys. Rev. D **109**, 114513 (2024).
[109] S. Rodini and A. Vladimirov, J. High Energy Phys. 09 (2023) 117.
[110] H. T. Shu, M. Schlemmer, T. Sizmann, A. Vladimirov, L. Walter, M. Engelhardt, A. Schäfer, and Y. B. Yang, Phys. Rev. D **108**, 074519 (2023).
[111] M. H. Chu *et al.* (Lattice Parton Collaboration), Phys. Rev. D **109**, L091503 (2024).
[112] Ó. del Río and A. Vladimirov, Phys. Rev. D **108**, 114009 (2023).
[113] M. H. Chu *et al.* (Lattice Parton Collaboration (LPC)), J. High Energy Phys. 08 (2023) 172.

[114] C. Alexandrou, S. Bacchio, K. Cichy, M. Constantinou, X. Feng, K. Jansen, C. Liu, A. Sen, G. Spanoudes, F. Steffens *et al.*, Phys. Rev. D **108**, 114503 (2023).
[115] A. Avkhadiev, P. E. Shanahan, M. L. Wagman, and Y. Zhao, Phys. Rev. D **108**, 114505 (2023).
[116] Y. Zhao, Phys. Rev. Lett. **133**, 241904 (2024).
[117] A. Avkhadiev, P. E. Shanahan, M. L. Wagman, and Y. Zhao, Phys. Rev. Lett. **132**, 231901 (2024).
[118] D. Bollweg, X. Gao, S. Mukherjee, and Y. Zhao, Phys. Lett. B **852**, 138617 (2024).
[119] G. Spanoudes, M. Constantinou, and H. Panagopoulos, Phys. Rev. D **109**, 114501 (2024).
[120] J. H. Zhang, arXiv:2304.12481.
[121] M. Jaarsma, R. Rahn, and W. J. Waalewijn, J. High Energy Phys. 12 (2023) 014.
[122] V. Braun, R. J. Fries, N. Mahnke, and E. Stein, Nucl. Phys. **B589**, 381 (2000); **B607**, 433(E) (2001).
[123] J. H. Zhang *et al.* (LP3 Collaboration), Nucl. Phys. **B939**, 429 (2019).
[124] G. Martinelli, C. Pittori, C. T. Sachrajda, M. Testa, and A. Vladikas, Nucl. Phys. **B445**, 81 (1995).
[125] X. Ji, Y. Liu, A. Schäfer, W. Wang, Y. B. Yang, J. H. Zhang, and Y. Zhao, Nucl. Phys. **B964**, 115311 (2021).
[126] Y. K. Huo *et al.* (Lattice Parton Collaboration (LPC)), Nucl. Phys. **B969**, 115443 (2021).
[127] K. Zhang, Y.-K. Huo, X. Ji, A. Schäfer, C.-J. Shi, P. Sun, W. Wang, Y.-B. Yang, and J.-H. Zhang (Lattice Parton Collaboration), Phys. Rev. D **110**, 074505 (2024).
[128] Z. C. Hu *et al.* (CLQCD Collaboration), Phys. Rev. D **109**, 054507 (2024).
[129] H. Liu, J. He, L. Liu, P. Sun, W. Wang, Y. B. Yang, and Q. A. Zhang, Sci. China Phys. Mech. Astron. **67**, 211011 (2024).
[130] H. Xing, J. Liang, L. Liu, P. Sun, and Y. B. Yang, arXiv:2210.08555.
[131] H. Yan, C. Liu, L. Liu, Y. Meng, and H. Xing, Phys. Rev. D **111**, 014503 (2025).
[132] Q. A. Zhang, J. Hua, F. Huang, R. Li, Y. Li, C. Lü, C. D. Lu, P. Sun, W. Sun, W. Wang, and Yibo Yang, Chin. Phys. C **46**, 011002 (2022).
[133] H. Liu, L. Liu, P. Sun, W. Sun, J. X. Tan, W. Wang, Y. B. Yang, and Q. A. Zhang, Phys. Lett. B **841**, 137941 (2023).
[134] H. Liu, W. Wang, and Q. A. Zhang, Phys. Rev. D **109**, 036037 (2024).
[135] Y. Meng, J. L. Dang, C. Liu, X. Y. Tuo, H. Yan, Y. B. Yang, and K. L. Zhang, Phys. Rev. D **110**, 074510 (2024).
[136] H. Y. Du *et al.* (CLQCD Collaboration), arXiv:2408.03548.
[137] D. J. Zhao, G. Wang, F. He, L. Jin, P. Sun, Y.-B. Yang, and K. Zhang (χQCD Collaboration), Phys. Rev. D **107**, L091501 (2023).
[138] X.-L. Meng, P. Sun, A. Alexandru, I. Horváth, K.-F. Liu, G. Wang, and Y.-B. Yang (χQCD and CLQCD Collaborations), J. High Energy Phys. 12 (2024) 101.
[139] G. S. Bali, B. Lang, B. U. Musch, and A. Schäfer, Phys. Rev. D **93**, 094515 (2016).
[140] M. Albanese *et al.* (APE Collaboration), Phys. Lett. B **192**, 163 (1987).
[141] R. Aaij *et al.* (LHCb Collaboration), J. High Energy Phys. 06 (2015) 115; 09 (2018) 145(E).
[142] R. G. Edwards, and B. Joó (SciDAC, LHPC, and UKQCD Collaborations), Nucl. Phys. B, Proc. Suppl. **140**, 832 (2005).
[143] M. A. Clark, R. Babich, K. Barros, R. C. Brower, and C. Rebbi (QUDA Collaboration), Comput. Phys. Commun. **181**, 1517 (2010).
[144] R. Babich *et al.* (QUDA Collaboration), Scaling lattice QCD beyond 100 GPUs, in *SC '11: Proceedings of the 2011 International Conference for High Performance Computing, Networking, Storage and Analysis* (2011), p. 70, 10.1145/2063384.2063478.
[145] M. A. Clark *et al.* (QUDA Collaboration), Accelerating lattice QCD multigrid on GPUs using fine-grained parallelization, in *Proceedings of the International Conference for High Performance Computing, Networking, Storage and Analysis (SC '16)* (2016), p. 68, 10.5555/3014904.3014995.
[146] Y. J. Bi, Y. Xiao, W. Y. Guo, M. Gong, P. Sun, S. Xu, and Y. B. Yang, Proc. Sci. LATTICE2019 (**2020**) 286 [arXiv:2001.05706].